

Chemically bonded carbon quantum dots/Bi₂WO₆ S-scheme heterojunction for boosted photocatalytic antibiotic degradation: Interfacial engineering and mechanism insight

Haitao Ren ^a, Fan Qi ^b, Abdelkader Labidi ^a, Junjun Zhao ^a, Hui Wang ^a, Yue Xin ^a, Jianmin Luo ^{c,*}, Chuanyi Wang ^{a,*}

^a School of Environmental Science and Engineering, Shaanxi University of Science and Technology, Xi'an 710021, PR China

^b State Key Laboratory of Medicinal Chemical, College of Pharmacy, Nankai University, Tianjin 300071, PR China

^c School of Chemistry and Civil Engineering, Shaoguan University, Shaoguan 512005, PR China



ARTICLE INFO

Keywords:

S-scheme heterojunction
Bismuth tungstate
Carbon quantum dots
Interfacial engineering
Visible light photocatalysis

ABSTRACT

Design of green and low-cost S-scheme heterojunctions with strong interface interactions is critical to their photocatalytic performance and practical application. Here, novel S-scheme heterojunctions of 0D/2D carbon quantum dots/Bi₂WO₆ (CQDs/Bi₂WO₆) were successfully fabricated by an in-situ hydrothermal process, where the CQDs were derived from waste biomass. The Bi-O-C bonds were formed at their interface, providing an atomic-level interfacial channel for promoting charge separation. As supported by work function calculations, in-situ X-ray photoelectron spectroscopy (XPS), and electron paramagnetic resonance (EPR) analyses, an S-scheme charge migration path was unveiled within the CQDs/Bi₂WO₆ during the photocatalytic reaction. The 3 wt% CQDs/Bi₂WO₆ S-scheme heterojunction displayed an optimal photocatalytic activity, which is 4.01 and 64.71 times higher than those of Bi₂WO₆ and CQDs, respectively. Based on theoretical calculations and experimental results, the photocatalytic mechanism, possible intermediates, and degradation pathways were enunciated. Furthermore, the non-toxicity of the developed heterojunction and degraded tetracycline solution was testified by *E.coli* cultivation.

1. Introduction

Antibiotic tetracycline (TC) has been extensively utilized to treat diseases from which humans, animals, and aquaculture suffer [1]. TC has high structural stability and resistance, making its complete metabolism by humans and animals and its degradation in natural environment difficult [2]. If entering the environment without effective purification, it will engender hazardous impacts on human health and the ecological environment. Therefore, developing a green and high-efficient strategy for TC removal is imminently demanded. As a safe, efficient, and sustainable purification technology, photocatalytic technology has aroused extensive interest [3]. Among various photocatalysts, Bi₂WO₆ is a representative perovskite oxide characterized by its unique lamellar structure, high stability, and suitable band gap of approximately 2.75 eV, which makes it suitable to work as a photocatalyst for pollutants removal [4,5]. However, the photocatalytic performance of pristine Bi₂WO₆ needs to be further improved because of its

low visible light utilization ($\lambda \leq 450$ nm), high electron-hole (e⁻-h⁺) recombination rate, and high conduction band (CB) position that limits its reduction ability [6].

To overcome the above-mentioned limitations of Bi₂WO₆-based photocatalysts, several strategies have been developed to boost their photocatalytic performances, including the construction of heterojunctions [7], the introduction of defects [8], control of morphology [9] and the loading of co-catalysts (such as noble metals) [10]. Among those strategies, fabricating heterojunctions has demonstrated to be advantageous in producing effective photocatalytic systems with a favorable visible light response, efficient charge separation as well as high redox ability [11,12], especially S-scheme heterojunctions. Recently, Yu's group proposed an innovative S-scheme heterojunction photocatalyst [13]. In the S-scheme heterojunction, it was demonstrated that when two semiconductors with different values in Fermi levels (E_F) are in contact, free electrons would move from the semiconductor with a high E_F to the other semiconductor with a low E_F until they are balanced at

* Corresponding authors.

E-mail addresses: xxyljm@163.com (J. Luo), wangchuanyi@sust.edu.cn (C. Wang).

their interfaces [14]. Thus, electron transfers would result in the creation of internal electric field (IEF) and band bending at their interfaces. Under light irradiation, driven by the IEF and bending band, effective separation of photoproduced charges can be achieved. The strongly reductive e^- and oxidative h^+ can also be reserved in the lower CB and higher valence band (VB), respectively [15]. Consequently, the construction of S-scheme heterojunction allows for enhancing the photocatalytic performance of the original Bi_2WO_6 . For instance, various Bi_2WO_6 -based S-scheme heterojunctions, such as CdS QDs/ Bi_2WO_6 [16], $\text{Cd}_{0.5}\text{Zn}_{0.5}\text{S}/\text{Bi}_2\text{WO}_6$ [17], $\text{Cs}_2\text{AgBiBr}_6/\text{Bi}_2\text{WO}_6$ [18] and $\text{Bi}_2\text{WO}_6/\text{g-C}_3\text{N}_4$ [19], have been developed for improved photocatalytic activity. Unfortunately, the most reported S-scheme heterojunctions still suffer from the following two issues: (1) lack of chemical bond level interface interaction leading to low charge transfer efficiency and poor stability; and (2) requiring complex synthesis processes, expensive or toxic raw materials, which hinders their long-term use and large-scale production. Therefore, it is necessary to develop green, inexpensive, and chemically bonded Bi_2WO_6 -based S-scheme heterojunctions that can be easily synthesized to promote their practical applications in the future.

Till now, carbon quantum dots (CQDs) have been widely used in designing photocatalysts due to their ultra-small size, quantum confinement effect, edge effect, and low-cost characters. For instance, CQDs/ TiO_2 , CQDs/ Bi_2MoO_6 , CQDs/ $\text{Bi}_2\text{WO}_6/\text{BiOBr}$, CQDs/ ZnIn_2S_4 , $\text{Bi}_2\text{MoO}_6/\text{CQDs}/\text{Bi}_2\text{S}_3$, and CQDs/g- C_3N_4 [20–24], etc., have been constructed. Among them, CQDs are used as co-catalysts to extend the light-responsive range, as well as to separate and migrate the photoproduced charges. Thus, employing CQDs to replace semiconductors or noble metals is an effective strategy to boost the photocatalytic activity of catalysts. Recent studies have proven that CQDs can also act as a semiconductor. When graphite is transformed into nano-carbon dots, its CB and VB are separated and a quantum confinement effect appears [25, 26]. For instance, Qin et al. constructed N-CQDs/ Sn_3O_4 heterojunctions to boost the degradation of methyl orange [27]. Wang et al. fabricated a Z-scheme N-CQDs/TNS-001 to enhance diclofenac degradation [28]. Zhao et al. described WO_3/CQDs nanohybrid with IEF to improve the degradation of volatile organic compounds [29]. Nevertheless, in previous studies, when CQDs were coupled with semiconductors, the actual interfacial charge transfer mechanism of the composites remains to be clarified, and more efforts are deserved for constructing a well-engineered interface to facilitate electron transfer towards improving photocatalytic performance.

In the present work, we constructed a novel S-scheme heterojunction of 0D/2D CQDs/ Bi_2WO_6 nanosheets by adding waste biomass-derived CQDs into the system of Bi_2WO_6 , which avoids the use of expensive and polluting chemicals to a large extent (Scheme 1). Interestingly, Bi-O-C bonds were formed in the heterojunction, which endows heterojunctions with more intimate connection and thereby provides an atomic-level interfacial channel for promoting charge separation. Under

visible light, the e^- in the CB of Bi_2WO_6 would readily recombine with the h^+ in the VB of CQDs, following an S-scheme charge migration pathway. As a result, the 3 wt% CQDs/ Bi_2WO_6 heterojunction displayed superior photocatalytic performance for TC degradation, showing 4.01 and 64.71 times higher activity than those of pristine Bi_2WO_6 and CQDs, respectively. Furthermore, favorable stability and adaptability of 3 wt% CQDs/ Bi_2WO_6 heterojunction were proved during the photocatalytic process. The non-toxicity of the developed heterojunction and treated TC solution, photocatalytic mechanism, and degradation pathways were also elucidated.

2. Experimental

2.1. Materials

The used chemicals and reagents are given in [Supplementary Information \(SI\) \(Text S1\)](#).

2.2. Characterizations

The characterization techniques of the as-obtained catalysts are given in SI (Text S2).

2.3. Synthesis of CQDs derived from biomass waste

The biomass waste of peach leaves was washed several times with ultrapure water and dried at 80 °C. The dried peach leaves were grounded into a powder. 0.5 g of fine powder was blended with 60 mL ultrapure water. Subsequently, the homogenous mixture was added to a 100 mL autoclave and heated at 240 °C for 6 h. Afterwards, the autoclave was naturally cooled at ambient temperature. Then, the nut-brown liquid mixture was filtered many times by way of a 50 nm membrane filter to separate the solution containing CQDs. Eventually, the brownish-yellow CQDs solution was obtained and freeze-dried to collect the CQDs powder to conduct further experiments.

2.4. Synthesis of CQDs/ Bi_2WO_6 heterojunction

2.0 mmol of $\text{Bi}(\text{NO}_3)_3 \cdot 5 \text{H}_2\text{O}$ was mixed with 15 mL of 1.0 mol·L⁻¹ HNO_3 solution. Then, the mixture was constantly mixed at ambient temperature for 20 min (solution A). Meanwhile, solution B was obtained by dissolving 1.0 mmol of $\text{Na}_2\text{WO}_4 \cdot 2 \text{H}_2\text{O}$ in 10 mL of ultrapure water. The prepared solution was sonicated for 10 min. Later, specific amounts of CQDs (0.007, 0.021, 0.035, and 0.049 g) were solubilized in 10 mL of ultrapure water and sonicated for 20 min to form solutions (C₁-C₄). After that, solutions A and B were added to C₁-C₄ separately and mixed under continuous magnetic stirring for 30 min. Their pH was regulated to 2.0 using 1.0 mol·L⁻¹ NaOH solution. The precursor solutions were transferred into 50 mL of autoclave and heated at 180 °C for 24 h. After natural cooling at ambient temperature, the fine powder of each solution was separated from the liquid mixture by centrifugation at 10,000 rpm for 5 min. Afterwards, the obtained products were washed three times using ultrapure water and ethanol successively. Finally, the samples containing different amounts of CQDs and denoted respectively by 1 wt% CQDs/ Bi_2WO_6 , 3 wt% CQDs/ Bi_2WO_6 , 5 wt% CQDs/ Bi_2WO_6 and 7 wt% CQDs/ Bi_2WO_6 were dried at 60 °C for 12 h. Additionally, pristine Bi_2WO_6 was synthesized following the same process by excluding the addition of CQDs.

2.5. Photocatalytic activity evaluation

The photocatalytic activity was evaluated by degrading TC, and the experimental details were supplied in SI (Text S3).



Scheme 1. Schematic illustration for the construction of S-scheme CQDs/ Bi_2WO_6 heterojunction.

2.6. The influence of photon absorption on photocatalytic activity

To evaluate the influence of catalyst optical parameters, reactor optical thickness, and the total rate of photon absorption (TRPA) on photocatalytic activity, photodegradation experiments were conducted in a planar reactor by varying the incident light intensities (70–100 mW/cm²) and suspension depths (2 and 4 cm) [30–32]. Based on previous studies by G. Li Puma et al., the six-flux absorption scattering model (SFM) was used to estimate the spatial distribution of the local volume photon absorption rate (LVRPA) in the planar reactor, as depicted in Eq. (1) [33]:

$$e^a(x) = \frac{I_0 \tau_{app}}{\omega_{corr}(1-\gamma)L} \left[\left(\omega_{corr} - 1 + \sqrt{1 - \omega_{corr}^2} \right) e^{-x\tau_{app}/L} + \gamma \left(\omega_{corr} - 1 - \sqrt{1 - \omega_{corr}^2} \right) e^{x\tau_{app}/L} \right] \quad (1)$$

where a , b , ω_{corr} , and γ are SFM parameters described as follows:

$$a = 1 - \omega p_f - \frac{4\omega^2 p_s^2}{1 - \omega p_f - \omega p_b - 2\omega p_s} \quad (2)$$

$$b = \omega p_b + \frac{4\omega^2 p_s^2}{1 - \omega p_f - \omega p_b - 2\omega p_s} \quad (3)$$

$$\omega_{corr} = \frac{b}{a} \quad (4)$$

$$\gamma = \frac{1 - \sqrt{1 - \omega_{corr}^2}}{1 + \sqrt{1 - \omega_{corr}^2}} e^{-2\tau_{app}} \quad (5)$$

the apparent optical thickness τ_{app} is:

$$\tau_{app} = a\tau\sqrt{1 - \omega_{corr}^2} \quad (6)$$

the apparent scattering albedo ω is:

$$\omega = \frac{\sigma}{\beta} = \frac{\sigma}{\sigma + k} \quad (7)$$

and the optical thickness τ is:

$$\tau = \beta C_{cat} L = (\sigma + k) C_{cat} L \quad (8)$$

where β , σ and k are the catalyst specific extinction, scattering and absorption coefficients, determined by previously reported method [34]; C_{cat} and L are the catalyst concentration and the depth of solution in the planar reactor, respectively. The p_f , p_b and p_s represent the probability of scattering forward, backward and sideward, respectively, which were defined by referring to the procedure depicted by G. Li Puma et al. [35].

The total rate of photon absorption (TRPA) is the entire radiation absorbed within the overall reactor volume [36], which was computed by integrating the LVRPA over the depth of the planar reactor. The TRPA per unit surface area is:

$$TRPA / A = \int_0^L e^a(x) dx \quad (9)$$

2.7. Biotoxicity assessment

Typical Gram-negative bacteria *Escherichia coli* (*E. coli*) was selected as a biological subsequent model used to assess the toxicity of catalysts and the degraded solutions of TC, and a detailed process of toxicity tests was given in SI (Text S4).

2.8. Theoretical calculations

The work functions of Bi_2WO_6 and CQDs were calculated by the MedeA@VASP software package and the calculation details were

outlined in SI (Text S5). Additionally, the density functional theory (DFT) calculations of TC were carried out using the Gaussian 9 software package. The geometric structure optimization of TC was determined with the B3LYP functional at the 6–31 +G (d, p) basis set. The Fukui index according to the Hirshfeld charge and the electrostatic potential (ESP) of TC was obtained by Multiwin 3.8.

3. Results and discussion

3.1. Material characterization

The morphological features and microstructures of the obtained catalysts were analyzed using SEM, TEM, and HR-TEM. The CQDs displays a spherical shape with an average size of 4.73 nm (Fig. S1) and a lattice spacing of 0.327 nm (inset of Fig. S1), which is associated with the (002) plane of graphite carbon [5]. This result demonstrates that the CQDs with favorable crystallinity were synthesized from waste peach leaves by hydrothermal processing. In Fig. 1a, pure Bi_2WO_6 displays a 2D irregular petal-like morphology consisting of small particles with a diameter range of 50–80 nm. With the introduction of CQDs, the 3 wt% CQDs/ Bi_2WO_6 exhibits a 2D regular sheet-like structure with a diameter range of 80–150 nm (Fig. 1b and c), indicating that the added CQDs affected the growth orientation of Bi_2WO_6 in the hydrothermal process. Fig. 1d shows the small spheroidal particles embedded into the surface of Bi_2WO_6 nanosheets, suggesting their favorable interactions. Moreover, the HR-TEM image of 3 wt% CQDs/ Bi_2WO_6 (Fig. 1e) exhibits distinct lattice spacings of 0.272 nm and 0.327 nm, which respectively correspond to the (002) crystal face of CQDs and the (002) lattice plane of Bi_2WO_6 [37], revealing the successful bonding of the CQDs with Bi_2WO_6 . Additionally, both crystal lattices with dissimilar orientations are coalesced at the junction (marked with a yellow dashed frame in Fig. 1e), indicating that intimate interactions are established between Bi_2WO_6 and CQDs at their interfaces [38]. The EDX elemental mapping images indicate that Bi, W, O, and C elements are evenly distributed in the 3 wt% CQDs/ Bi_2WO_6 composite (Fig. 1f and S2). The crystal structure of the Bi_2WO_6 and CQDs/ Bi_2WO_6 composites were analyzed by XRD (Fig. 1g). The characteristic diffraction peaks of the studied powders at 28.3°, 32.8°/32.9°, 47.1°, 56.0°, 58.5° and 68.8° can be assigned to the (131), (002), (202), (133), (262) and (400) crystal planes of Bi_2WO_6 (JCPDS No. 79–2381) [39], respectively. These observations indicate the successful preparation of Bi_2WO_6 . Moreover, signals about CQDs in composites containing more than 5% CQDs were observed (See the red arrow in Fig. 1g). By comparison, no CQDs diffraction peaks are detected in composites containing less than 5% CQDs because of the low CQDs content in the composites [40]. Moreover, the predominant peak (28.3°) and secondary peak (32.9°) of CQDs/ Bi_2WO_6 heterostructure are weaker in intensity compared to pure Bi_2WO_6 , demonstrating that the addition of CQDs affects the crystal orientation of Bi_2WO_6 , which is consistent with the SEM result.

The surface chemical states and the compositions of Bi_2WO_6 and 3 wt% CQDs/ Bi_2WO_6 composites were further analyzed by XPS. As displayed in Fig. 2a, the survey spectrum shows the existence of Bi, W, O, and C atoms in 3 wt% CQDs/ Bi_2WO_6 composite. For the Bi_2WO_6 , the XPS spectra of Bi4f display two peaks at 164.5 and 159.2 eV, corresponding to Bi4f5/2 and Bi4f7/2 of Bi_2WO_6 , respectively (Fig. 2b) [41]. In addition, two new peaks emerge at the binding energies of 157.9 and 163.3 eV, denoting that the Bi–O–C bond is established between Bi_2WO_6 and CQDs [42]. The peaks of the W4f spectrum of Bi_2WO_6 (Fig. 2c) at 37.6 and 35.5 eV are assigned to W4f5/2 and W4f7/2, respectively [5, 43]. Compared to pure Bi_2WO_6 , the peaks of Bi4f and W4f in 3 wt% CQDs/ Bi_2WO_6 composite shift toward lower binding energy, implying that the electron density in Bi_2WO_6 is increased by forming well-designed heterojunction. The O1s peaks of Bi_2WO_6 at 530.1 and 531.9 eV (Fig. 2d) can be assigned to the crystal lattice oxygen and the adsorbed oxygen from H_2O , respectively [5, 44]. For the 3 wt% CQDs/ Bi_2WO_6 , two extra peaks appear at 531.1 and 532.7 eV that can

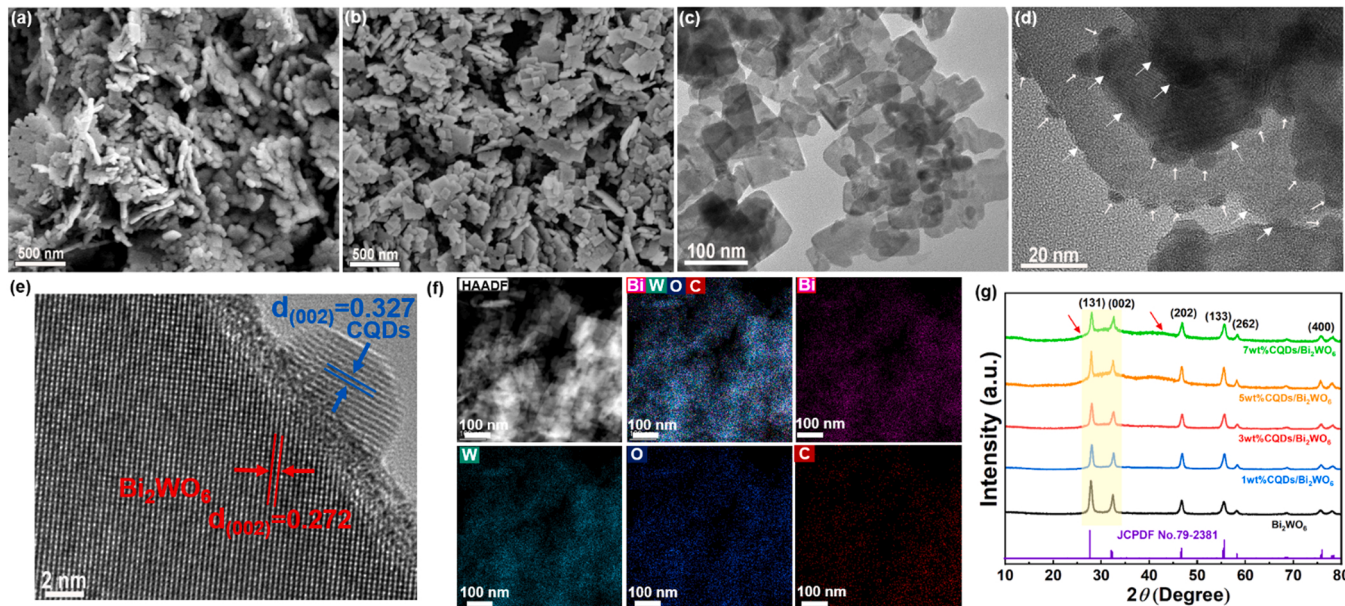


Fig. 1. FE-SEM images of (a) Bi_2WO_6 and (b) 3 wt% CQDs/ Bi_2WO_6 . (c, d) TEM and (e) HR-TEM images of 3 wt% CQDs/ Bi_2WO_6 . (f) TEM image and the associated EDX elemental maps of 3 wt% CQDs/ Bi_2WO_6 . (g) XRD patterns of Bi_2WO_6 and CQDs/ Bi_2WO_6 .

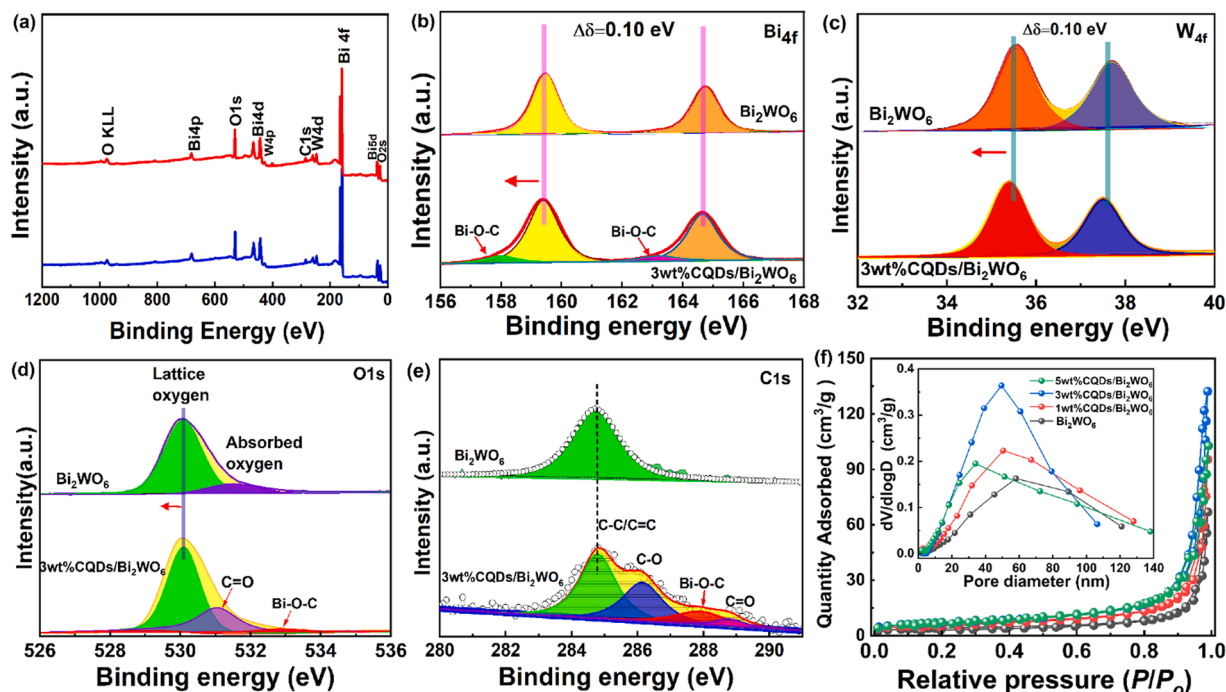


Fig. 2. (a) XPS survey spectra, (b) Bi4f spectra, (c) W4f spectra, (d) O1s spectra, (e) C1s spectra of Bi_2WO_6 and 3 wt% CQDs/ Bi_2WO_6 composites. (f) N_2 adsorption-desorption isotherms and pore size distribution (inset) of Bi_2WO_6 and CQDs/ Bi_2WO_6 composites.

be attributed to the C=O and C-O-Bi, indicating the existence of CQDs and the interfacial chemical bonding formation, respectively [45]. Additionally, as presented in Fig. 2e, the C1s peak located at 284.8 eV in pure Bi_2WO_6 is ascribed to the compensated carbon from the XPS instrument during the test. The C1s spectrum of 3 wt% CQDs/ Bi_2WO_6 (Fig. 2e) is divided into four peaks. The peaks positioned at 284.8, 286.2, 288.0, and 288.9 eV are respectively attributed to C-C/C=C, C-O, Bi-O-C, and C=O bonds, demonstrating that 3 wt% CQDs/ Bi_2WO_6 composite inherited oxygen-containing groups such as hydroxyl (-OH) and carbonyl (C=O) groups from obtained CQDs. The presence of these groups facilitates the formation of a reliable heterointerface [42,45].

Notably, compared to pure Bi_2WO_6 , Bi-O-C bonds appear in XPS Bi4f, O1s, and C1s spectra of 3 wt% CQDs/ Bi_2WO_6 composite. The formation of Bi-O-C bonds renders the intense chemical interactions in the CQDs/ Bi_2WO_6 heterointerface, allowing fast electron migration and ensuring the structural stability of CQDs/ Bi_2WO_6 . Overall, these findings demonstrate the favorable interactions between Bi_2WO_6 and CQDs through an intense Bi-O-C bonding, revealing the huge potentiality of CQDs/ Bi_2WO_6 composite as a high-efficient photocatalyst.

Furthermore, the pore structure and specific surface area of as-synthesized catalysts were investigated. As shown in Fig. 2f and Table S1, the isotherms of all catalysts are type IV hysteresis loops,

indicating the presence of typical mesoporous nanostructure [46]. The pristine Bi_2WO_6 , 1 wt% CQDs/ Bi_2WO_6 , 3 wt% CQDs/ Bi_2WO_6 , and 5 wt% CQDs/ Bi_2WO_6 have specific surface areas of 19.02, 28.61, 35.48, and 35.56 $\text{m}^2\cdot\text{g}^{-1}$, mean pore sizes of 35.12, 29.71, 33.26, and 25.67 nm, respectively. These results indicate that the specific surface area of Bi_2WO_6 can be improved by adding CQDs. Increased specific surface area is beneficial to providing more adsorption and reaction sites toward the enhancement of photocatalytic performance in removing TC.

3.2. Photocatalytic TC degradation performance

First, the adsorption capacity of the catalysts for TC was assessed. As displayed in Fig. S3, after 30 min of the dark adsorption, the adsorption equilibrium can be achieved. Afterwards, the impact of catalyst concentration on the degradation of TC was explored. In Fig. S4, the degradation rate enhanced gradually with an increase in the catalyst concentration. When the catalyst concentration is 0.6 $\text{g}\cdot\text{L}^{-1}$, the degradation rate at 3 wt% CQDs/ Bi_2WO_6 achieved an optimum. With a further increase in catalyst concentration, there are no conspicuous changes in degradation rate, and the photocatalytic efficiency even somewhat reduced. This is due to the excessive catalyst making the solution opaque, thereby impeding the absorption of light. Hence, the optimal catalyst concentration of 0.6 $\text{g}\cdot\text{L}^{-1}$ was applied in the degradation experiments.

Furthermore, the photocatalytic performance of catalysts was investigated under visible light (Fig. 3a). The blank test proves that the TC can't be degraded without the presence of catalysts, signifying that the photodegradation of TC can be disregarded. Only 10% of TC is removed by pure CQDs in 40 min. Interestingly, compositing CQDs with Bi_2WO_6 remarkably enhanced the photocatalytic performance for TC removal. Fig. 3a reveals that the degradation efficiency of TC increases with adding CQDs in a certain amount, and decreases when further increasing the loading content of CQDs. This is due to its aggregation on the surface of Bi_2WO_6 , which shields Bi_2WO_6 to absorb visible light and covers the catalytic reactive sites [47]. The 3 wt% CQDs/ Bi_2WO_6 shows the highest photocatalytic efficiency for TC degradation (89.0%) within 40 min, which is higher than that of pristine Bi_2WO_6 (69.0%). The

photocatalytic degradation kinetics of TC was explored by the pseudo-first-order model with the formula: $-\ln\frac{C}{C_0} = k_1 t$ and pseudo-second-order model applying the following formula: $\frac{1}{C} = k_2 t + \frac{1}{C_0}$ [48]. The rate constants for both kinetic models are given in Table S2. The correlation coefficient (R^2) shows that the photocatalytic degradation of TC in the present work follows the pseudo-second-order kinetic model (Fig. 3b). Fig. 3c reveals that the k_2 value of 3 wt% CQDs/ Bi_2WO_6 for degrading TC is 0.3132 $\text{L}\cdot\text{mg}^{-1}\cdot\text{min}^{-1}$, which is 4.01 and 64.71 times higher than those of pure Bi_2WO_6 (0.0781 $\text{L}\cdot\text{mg}^{-1}\cdot\text{min}^{-1}$) and CQDs (0.0048 $\text{L}\cdot\text{mg}^{-1}\cdot\text{min}^{-1}$), respectively. Fig. 3d illustrates the variation of the absorption spectra of TC degradation within different irradiation times using 3 wt% CQDs/ Bi_2WO_6 . The absorption intensity at 356 nm corresponding to the maximum absorbance of TC weakens gradually with the reaction time, suggesting that TC molecules are destructed during the visible light driven photocatalytic reaction process. Besides, Fig. S5 displays the TOC removal efficiency of TC over Bi_2WO_6 and 3 wt% CQDs/ Bi_2WO_6 under visible light. The 3 wt% CQDs/ Bi_2WO_6 has a high mineralization efficiency of 48.5% after 1.0 h of illumination, which is 2.76 times more than that of pure Bi_2WO_6 (17.6%). This result proves that 3 wt% CQDs/ Bi_2WO_6 can mineralize TC more efficiently. Moreover, 3 wt% CQDs/ Bi_2WO_6 was compared with other photocatalysts for TC degradation. As given in Table S3, the photocatalytic activity of the 3 wt% CQDs/ Bi_2WO_6 catalyst developed in the present work is advantageous compared to the previously reported photocatalysts, demonstrating its great potential for antibiotic product degradation in wastewater.

To appraise the influence of photon absorption on the photocatalytic activity of 3 wt% CQDs/ Bi_2WO_6 , experiments were executed at different light intensities at suspension depths of 2 and 4 cm. At 2 cm: 70 mW/cm^2 (TPRA/A=629 W/m^2), 80 mW/cm^2 (TPRA/A=718 W/m^2), 90 mW/cm^2 (TPRA/A=808 W/m^2) and 100 mW/cm^2 (TPRA/A=898 W/m^2). At 4 cm: 70 mW/cm^2 (TPRA/A=586 W/m^2), 80 mW/cm^2 (TPRA/A=670 W/m^2), 90 mW/cm^2 (TPRA/A=754 W/m^2) and 100 mW/cm^2 (TPRA/A=838 W/m^2). The optical parameters of the catalysts are shown in Table S4. Fig. 4a displays that for a specific value of suspension depth, the larger the incident light intensity, the higher the efficiency of TC degradation. This is due to more absorption of photons by 3 wt% CQDs/ Bi_2WO_6 and the more generation of active

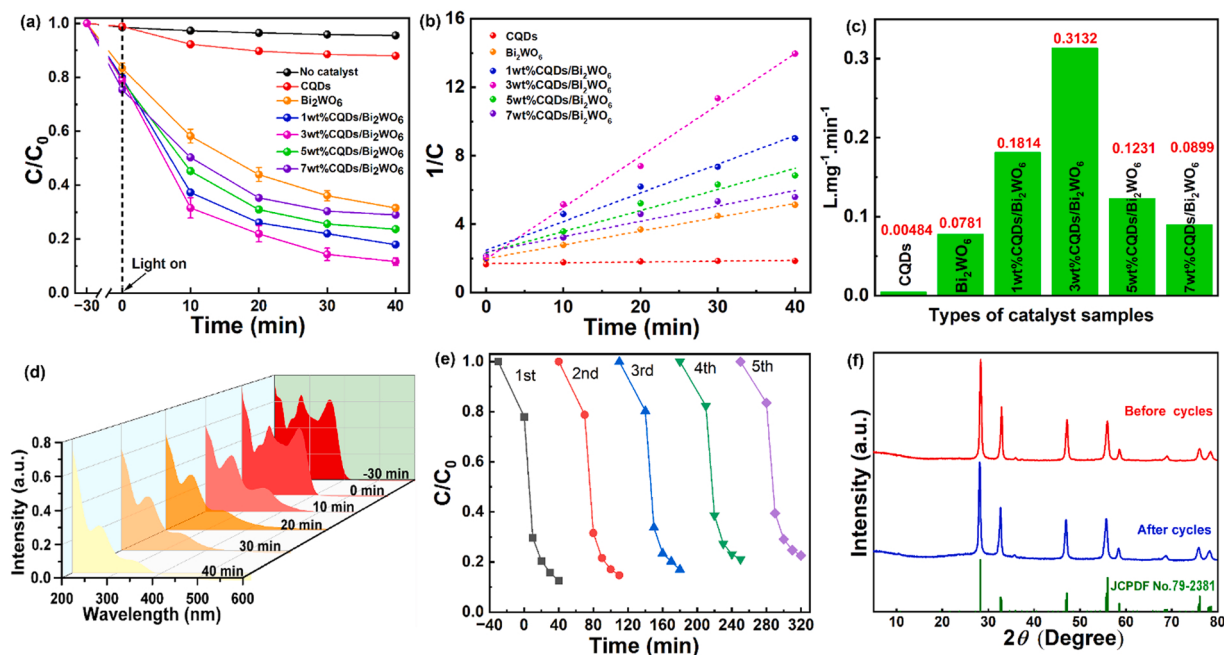


Fig. 3. (a) Performance curves, (b) plots of $1/C$ versus irradiation time, (c) rate constants of TC degradation over various catalysts. (d) UV-vis absorption spectral evolution of TC over 3 wt% CQDs/ Bi_2WO_6 . (e) Photocatalytic degradation of TC by 3 wt% CQDs/ Bi_2WO_6 in five consecutive runs. (f) XRD patterns of 3 wt% CQDs/ Bi_2WO_6 after five successive cycles.

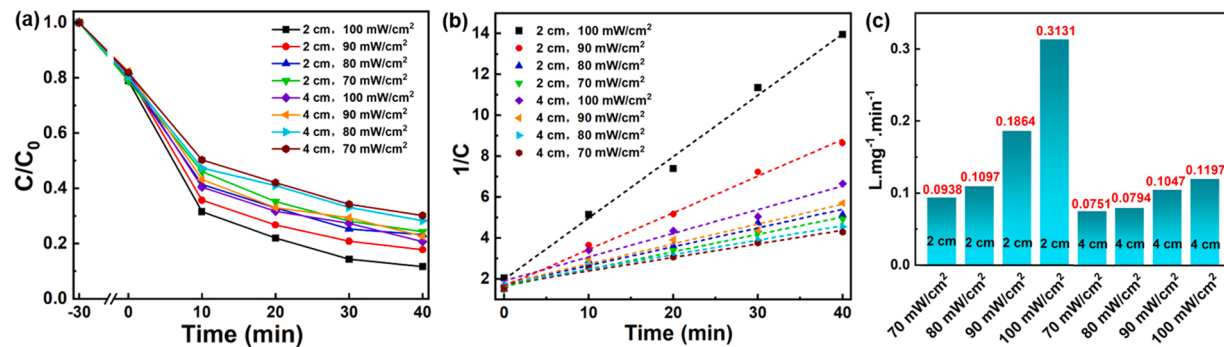


Fig. 4. (a) Performance curves, (b) plots of $1/C$ versus irradiation time, and (c) corresponding rate constants of TC degradation over 3 wt%CQDs/Bi₂WO₆ under different light intensities and solution depths.

species. Besides, for a specific value of light intensity, TRPA reduces with increasing suspension depth, and thus the degradation efficiency is slower when the suspension depth is 4 cm. For example, at a suspension depth of 2 cm, the degradation efficiency of TC is 75.5% and 89.0% in the 70 and 100 mW/cm² intensity, respectively. After irradiation with 100 mW/cm² intensity, the degradation efficiency of TC is 89.0% and 79.8% in the 2 and 4 cm suspension depth, respectively. In Fig. 4b and c, the degradation rate constants of TC increased with rising TRPA, and it should be noted that the phenomenon is light-limited within the extent of TRPA values investigated. Furthermore, concentration of catalyst was maintained at 0.6 g·L⁻¹. According to Eq. (8), the maximum optical thickness of the reactor was calculated to be 2.6, corresponding to a liquid depth of 4 cm. In contrast, this value is 1.3 when the liquid depth is 2 cm. As shown in Fig. 4a-c, under the same conditions, the degradation efficiency of TC at 2 cm liquid depth is greater than that at 4 cm liquid depth. Thus, the optimum optical thickness of the reactor is 1.3, and it was used in the degradation experiments under the irradiation intensity of 100 mW/cm².

3.3. Reusability, stability, and adaptability of 3 wt%CQDs/Bi₂WO₆

To assess the reusability and stability of the 3 wt%CQDs/Bi₂WO₆, cycling experiments were performed under visible light. At each cycle, the photocatalyst was washed, centrifuged, dried, and reused for TC degradation. In Fig. 3e, the photodegradation activity of 3 wt%CQDs/Bi₂WO₆ shows slight deactivation (with a decrease of < 8.5% after 5 cycles). The deactivation could be caused by the accumulation of uncleaned TC and intermediates on the surface of the 3 wt%CQDs/Bi₂WO₆ after multiple cycles. In addition, to assess the structural stability of the 3 wt%CQDs/Bi₂WO₆, the XRD analysis and TEM characterization of the 3 wt%CQDs/Bi₂WO₆ composite before and after the photodegradation process were performed. As displayed in Fig. 3f, the XRD patterns do not show apparent changes before and after the photocatalytic reaction, indicating that the 3 wt%CQDs/Bi₂WO₆ is stable during the photodegradation of TC. In addition, TEM and HR-TEM images (Fig. S6) confirm that the CQDs have remained in the 3 wt%CQDs/Bi₂WO₆ composite after the photocatalytic reaction, which further manifests the stability of the formed composite structure due to the strong interaction by forming Bi-O-C bonds between CQDs and Bi₂WO₆. Overall, the synthesized 3 wt%CQDs/Bi₂WO₆ composite exhibits favorable reusability and stable structure during 5 cycles in the photodegradation process.

To validate the ability of 3 wt%CQDs/Bi₂WO₆ to degrade pollutants of other properties, ciprofloxacin (CIP), bisphenol A (BPA), and rhodamine B (RhB) were further used as objects. As demonstrated in Fig. S7, the degradation efficiency of RhB, CIP, and BPA are 99.6%, 86.8%, and 80.5% within 1 h, respectively. The results indicate that 3 wt%CQDs/Bi₂WO₆ has favorable applicability for pollutants of other properties.

For practical applications of photocatalysts, some common anions, cations, and humic acid (HA) were introduced to the reaction solution to

explore their influence on the photocatalytic degradation of TC. As supported in Fig. S8, Cl⁻ and NO₃⁻ have little effect on the photocatalytic activity of 3 wt%CQDs/Bi₂WO₆, which may be due to that these two ions cannot impede the reaction of the TC with the active sites. However, the degradation efficiency of TC is slightly affected by the HA, CO₃²⁻ and SO₄²⁻. This is probably due to HA being adsorbed to the surface of 3 wt% CQDs/Bi₂WO₆ and shielding the active sites, thereby inhibiting the adsorption of TC to the surface of 3 wt%CQDs/Bi₂WO₆ [49]. Meanwhile, SO₄²⁻ can capture •OH generated by light excitation of 3 wt% CQDs/Bi₂WO₆, thus declining the photocatalytic activity [50]. Besides, the CO₃²⁻ can hydrolyze to produce OH⁻ and HCO₃⁻ ions, and excessive OH⁻ makes the degradation of TC more difficult. The CO₃²⁻ and HCO₃⁻ are also scavengers of active species [24,49]. In Fig. S9, the effect of cations on TC degradation was further investigated. After adding 10 mM Na⁺, K⁺, Mg²⁺, Ba²⁺, and Ca²⁺ to the reaction system, respectively, the degradation efficiency of TC is almost not affected. In addition, 3 wt% CQDs/Bi₂WO₆ remains a high degradation efficiency when the original pH ranges from 5.0 to 9.0 (Fig. S10), implying its favorable applicability in a broad pH operation range.

Furthermore, tap water, river water, and lake water were utilized to explore the application potential of 3 wt%CQDs/Bi₂WO₆ in actual aqueous mediums. The water quality parameters of the real water samples were illustrated in Table S5, including those of inorganic cations, organic matter, and pH. In Fig. S11, the degradation efficiency of TC by 3 wt%CQDs/Bi₂WO₆ in ultrapure water, tap water, river water, and lake water are 89.0%, 81.2%, 80.7%, and 79.4%, respectively, which suggests that the degradation of TC is slightly inhibited in real water samples. Through the above analysis, due to the inorganic cations and pH in the range of 5.0–9.0 have minor effect on TC degradation. This inhibition may be mainly caused by coexisting inorganic anions and organic compounds consuming a small part of catalytic reaction sites and active species [51]. Overall, these results demonstrate that the 3 wt%CQDs/Bi₂WO₆ has prevailing applicability in real water mediums.

3.4. Mechanism of TC photodegradation

The optical absorption of the catalysts was analyzed via UV-vis DRS in the wavelength range of 200–900 nm. As displayed in Fig. 5a, the absorption of CQDs/Bi₂WO₆ composites in the visible light region is enhanced relative to that of Bi₂WO₆, and increasing the content of CQDs leads to the color alteration from white to dark brown (the inset in Fig. 5a). This observation indicates that the CQDs/Bi₂WO₆ composites can absorb more solar light in favor of the photocatalytic activity for TC degradation. To interpret the promising superiority of CQDs in the broad-spectrum response of photocatalysts, the up-converted PL spectra of CQDs were inspected. In Fig. S12, the CQDs can emit short wavelengths of light, from 400 nm to 600 nm when excited with longer wavelength light, from 600 nm to 850 nm. The result evinces that CQDs have an up-conversion ability to transfer long-wavelength visible light

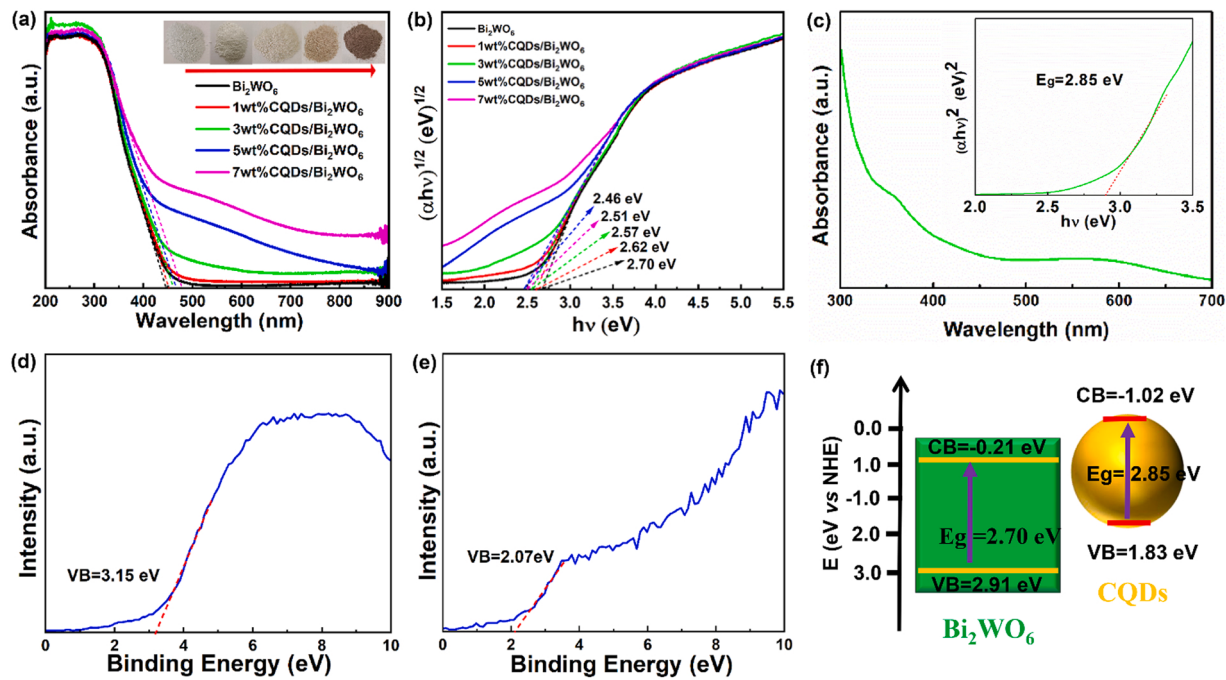


Fig. 5. (a) UV-vis DRS spectra and (b) Tauc plots of $(\alpha(hv))^{1/2}$ of Bi_2WO_6 and CQDs/ Bi_2WO_6 composites. (c) UV-vis DRS spectra of CQDs. Inset is the corresponding Tauc plot. VB-XPS spectra of (d) Bi_2WO_6 and (e) CQDs. (f) Band structure diagrams of Bi_2WO_6 and CQDs.

to short-wavelength visible light, implying that the CQDs/ Bi_2WO_6 photocatalyst can fully absorb the whole spectrum light to drive photocatalytic reactions. The band gap energies (E_g) can be estimated using Tauc plots: $(\alpha(hv))^{1/n} = A(hv - Eg)$, where α denotes the absorption coefficient, $h\nu$ represents the energy, A denotes the constant value, and $n = 2$ [39]. From Fig. 5b, the band gap energies of Bi_2WO_6 , 1 wt% CQDs/ Bi_2WO_6 , 3 wt% CQDs/ Bi_2WO_6 , 5 wt% CQDs/ Bi_2WO_6 , and 7 wt% CQDs/ Bi_2WO_6 were derived to be 2.70, 2.62, 2.57, 2.51, and 2.46 eV, respectively. As displayed in Fig. 5c, the absorption of CQDs is essentially bounded to the UV/blue range ($\lambda < 450$ nm), and the band gap energy of CQDs is 2.85 eV as derived from the corresponding Tauc plots described in the inset of Fig. 5c. The valence band potential of Bi_2WO_6 and CQDs was determined by a VB-XPS method. Fig. 5d and e display the VB-XPS spectra of Bi_2WO_6 and CQDs, in which VB values of Bi_2WO_6 and CQDs are 3.15 and 2.07 eV, respectively. Furthermore, the E_{VB} of the corresponding standard hydrogen electrode (E_{VB} vs. NHE) was estimated using the following equation (E_{VB} vs. NHE = $\Phi + E_{VB-XPS} - 4.44$) [51], where Φ is the electron work function of the instrument (4.20 eV). Consequently, the E_{VB} of Bi_2WO_6 and CQDs was derived to be 2.91 and 1.93 eV vs. NHE. Using the equation $E_g = E_{VB} - E_{CB}$, the E_{CB} of Bi_2WO_6 and CQDs was calculated to be -0.21 and -1.02 eV, respectively. The schematic diagram of the energy bands of Bi_2WO_6 and CQDs is displayed in Fig. 5f, suggesting the possible construction of S-scheme

heterojunction between Bi_2WO_6 and CQDs.

Generally, the separation and migration effectiveness of the photo-produced e^- - h^+ pairs are vital steps in the photocatalysis process. Therefore, photoelectric performance was evaluated by transient photocurrent responses, steady-state/time-resolved photoluminescence (PL) emission, and electrochemical impedance spectra (EIS). As depicted in Fig. 6a, the 3 wt% CQDs/ Bi_2WO_6 has the largest photocurrent density compared to the pure Bi_2WO_6 , suggesting that the combination of Bi_2WO_6 and CQDs promotes the separation of the photo-produced e^- - h^+ pairs [52]. Moreover, steady-state PL was employed to confirm the above results. Fig. 6b shows the PL spectra of Bi_2WO_6 and the CQDs/ Bi_2WO_6 composites, which show nearly the same shape when using the same excitation wavelength, i.e., 320 nm. However, the peak intensities decrease with adding CQDs and the lowest intensity is observed with the 3 wt% CQDs/ Bi_2WO_6 , which indicates that the introduction of CQDs plays a crucial role in avoiding the recombination of e^- and h^+ . The EIS spectra were also applied to further investigate charge transfer ability. In Fig. 6c, the 3 wt% CQDs/ Bi_2WO_6 exhibit the smallest semicircle of the EIS curve, indicating the lowest charge transfer resistance and best separation of the photo-produced e^- - h^+ pairs [53]. The interfacial separation capability of photo-produced charges can be further analyzed by time-resolved PL spectra. As shown in Fig. S13, the average lifetime of 3 wt% CQDs/ Bi_2WO_6 (3.25 ns) is longer than that

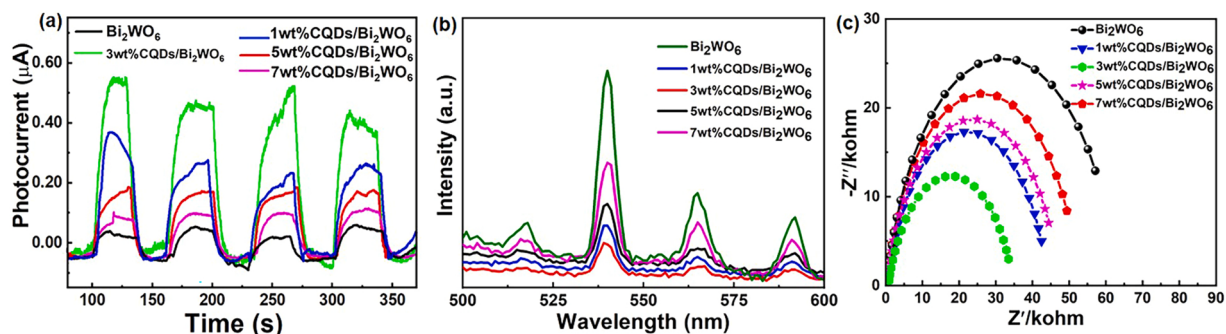


Fig. 6. (a) Transient photocurrent responses, (b) Photoluminescence spectra ($\lambda_{ex} = 320$ nm), and (c) Nyquist plots of Bi_2WO_6 and CQDs/ Bi_2WO_6 composites.

of Bi_2WO_6 (1.67 ns), which implies that the transportation of the photoproduced e^- between the CQDs and Bi_2WO_6 prolongs the carrier lifetime. This finding is in agreement with the results of transient photocurrent responses, PL spectra, and EIS analysis. Overall, these experimental results confirm that the interface interaction between Bi_2WO_6 and CQDs can facilitate the separation and transfer of the photoproduced e^- and h^+ and increase the lifetime of photoproduced carriers.

To elucidate the endogenous dynamics of photoproduced charge migration, as well as its type and direction between the Bi_2WO_6 and CQDs, the work functions (Φ) of Bi_2WO_6 and CQDs were determined based on DFT calculations. As shown in Fig. 7a and b, the Φ of Bi_2WO_6 and CQDs are determined to be 5.83 and 4.88 eV, respectively. Besides, the Φ of CQDs was further measured to be 4.86 eV by ultraviolet photoelectron spectroscopy (Fig. S14) [54], which is close to the DFT result. The Bi_2WO_6 has a high Φ and a low E_F , while CQDs have a small Φ and a high E_F . As displayed in Fig. 7c, when Bi_2WO_6 and CQDs are intimately contacted together, the e^- in CQDs will transfer to Bi_2WO_6 until achieving a balanced E_F [42,55]. This charge redistribution and high chemical interaction at interfaces can induce the formation of an IEF between the negatively charged Bi_2WO_6 and positively charged CQDs. In addition, the band edge of CQDs bends raised due to the loss of free electrons, while those of Bi_2WO_6 bends decreased due to the aggregation of free electrons. Under visible light irradiation, both Bi_2WO_6 and CQDs are excited, and the IEF and energy band bending drive the migration of photoproduced e^- from the CB of Bi_2WO_6 to combine with h^+ in the VB of CQDs. Consequently, the S-scheme heterojunction between Bi_2WO_6 and CQDs was successfully fabricated.

To further explore the interfacial interaction and charge transfer paths in 3 wt% CQDs/ Bi_2WO_6 during the photocatalytic process, an in-

situ XPS was conducted under visible light. In Fig. 8a and b, after light irradiation, the peaks of both W4f and Bi4f shift to higher binding energy, suggesting that elements W and Bi donate e^- under illumination. In Fig. 8b, the binding energy of the Bi-O-C bond increases, which proves that the photoproduced e^- transfer can be achieved through the Bi-O-C bond. In addition, in the O1s spectrum of 3 wt% CQDs/ Bi_2WO_6 (Fig. 8c), after light irradiation, the peak of the crystal lattice oxygen shifts to higher binding energy, while the peaks of the C=O and C-O-Bi bonds shift to the lower binding energy. This phenomenon may indicate that the photoproduced electrons are transferred from Bi_2WO_6 to CQDs by C-O-Bi bond channels. In the C1s spectrum of 3 wt% CQDs/ Bi_2WO_6 (Fig. 8d), the peak of the Bi-O-C bond shift to lower binding energy under irradiation, further indicating that the Bi-O-C bond can provide an e^- transfer channel in the heterojunction. Fig. 8e describes the interfacial chemical interaction and photoproduced e^- flow direction between Bi_2WO_6 and CQDs via the Bi-O-C bond. All these XPS results provide direct evidence of the e^- flow direction in 3 wt% CQDs/ Bi_2WO_6 , suggesting the successful construction of an S-scheme heterojunction between Bi_2WO_6 and CQDs.

To further unveil the photocatalytic reaction mechanism of TC by 3 wt% CQDs/ Bi_2WO_6 , the active species were identified by EPR spectroscopy during TC photodegradation. As shown in Fig. 9a and d, for CQDs, the EPR signal of $\bullet\text{O}_2$ can be detected. However, the signal of $\bullet\text{OH}$ is scarcely observed. Besides, as displayed in Fig. 9b and e, for Bi_2WO_6 , the signal of $\bullet\text{O}_2$ is negligible, while $\bullet\text{OH}$ signal can be identified. In contrast, as seen in Fig. 9c and f, after the introduction of CQDs on the Bi_2WO_6 , strong $\bullet\text{O}_2$ and $\bullet\text{OH}$ signals are observed, indicating more active species are produced in the 3 wt% CQDs/ Bi_2WO_6 photocatalytic system under visible light. To elucidate the contribution of specific reactive species to TC degradation, chemical quenching experiments

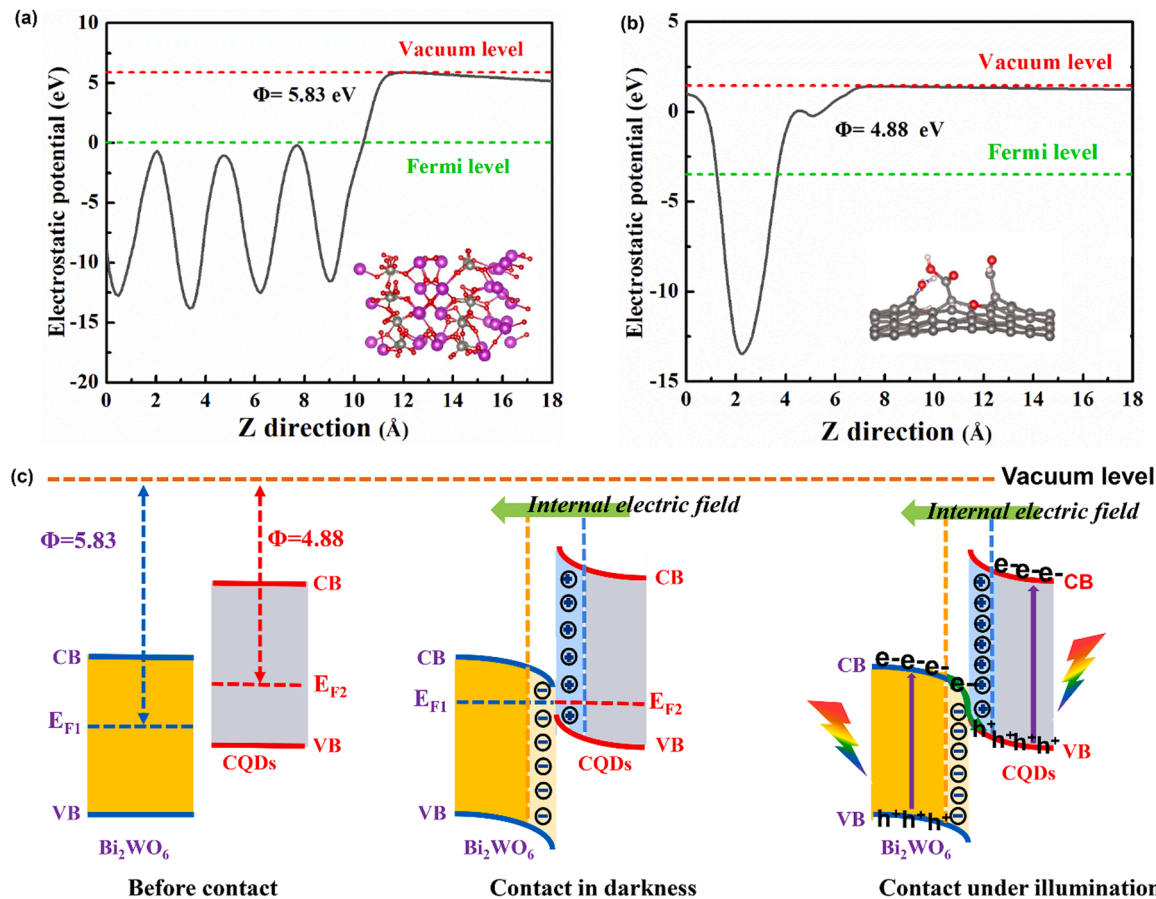


Fig. 7. Electrostatic potentials of (a) Bi_2WO_6 and (b) CQDs. (c) The energy band arrangements of Bi_2WO_6 and CQDs before contact, after contact in darkness, and contact under illumination.

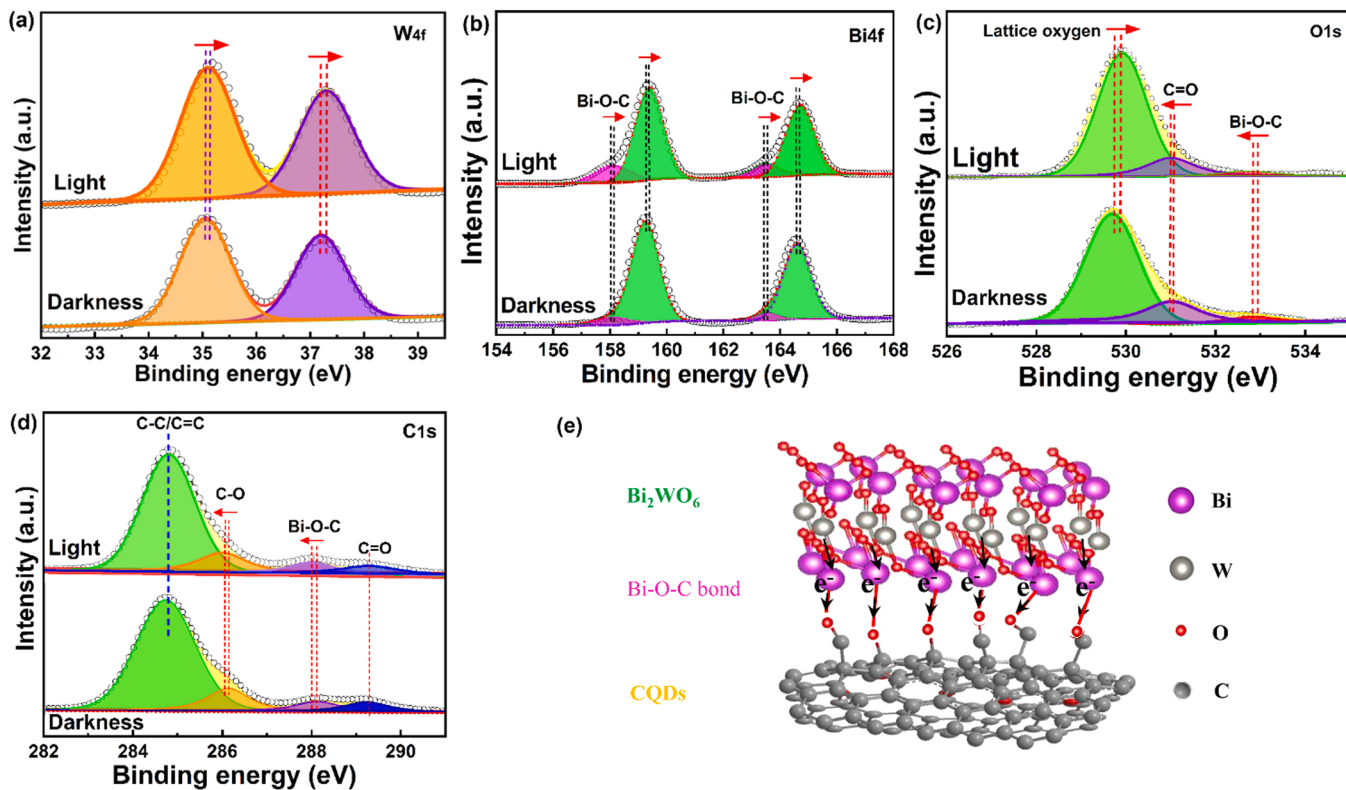


Fig. 8. In-situ XPS spectra for (a) W4f, (b) Bi4f, (c) O1s, and (d) C1s of 3 wt%CQDs/ Bi_2WO_6 in the dark and under visible light irradiation. (e) Schematic illustration of interfacial Bi-O-C bond between Bi_2WO_6 and CQDs.

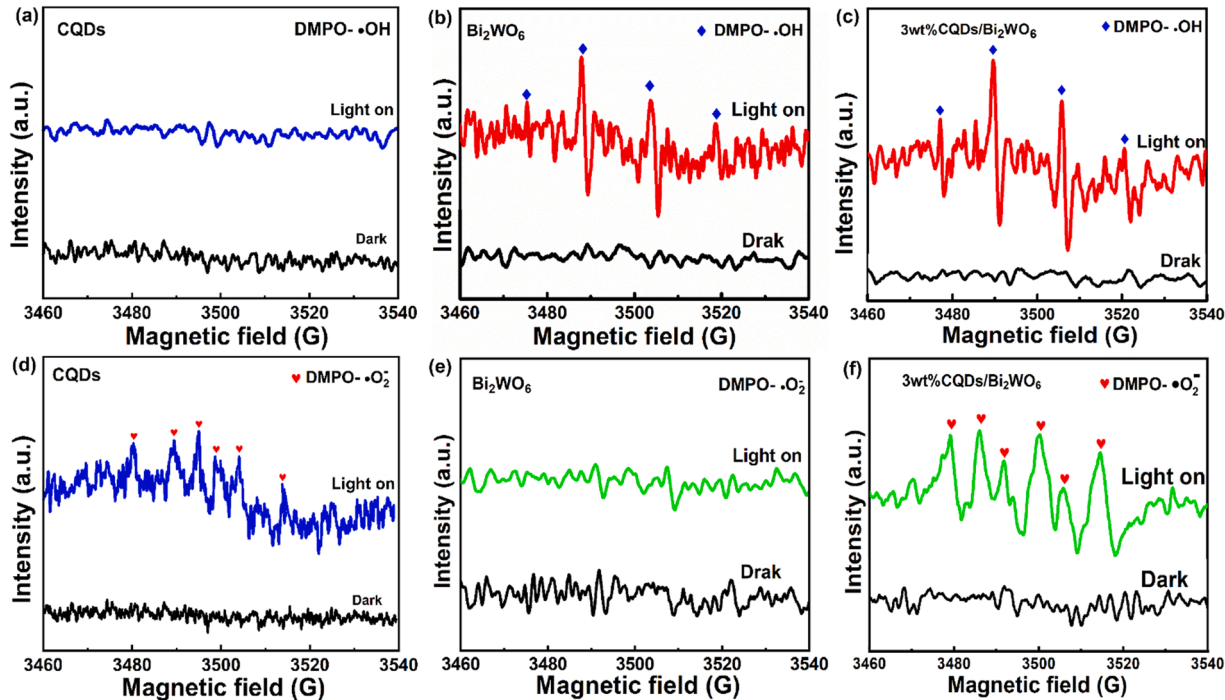


Fig. 9. EPR signals of CQDs, Bi_2WO_6 , and 3 wt%CQDs/ Bi_2WO_6 by DMPO-•OH (a, b and c) and DMPO-•O₂⁻ (d, e, and f).

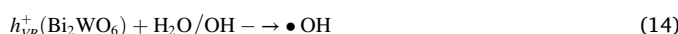
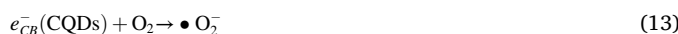
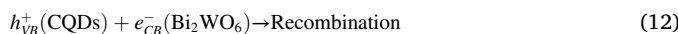
were performed. BQ, TBA and NaC_2O_4 act as quenchers of $\bullet\text{O}_2^-$, $\bullet\text{OH}$ and h^+ , respectively [56]. As displayed in Fig. S15, the degradation rate of TC (53.5%) is severely impeded after the introduction of BQ. With addition of TBA and $\text{Na}_2\text{C}_2\text{O}_4$, the degradation rate of TC decreased to some extent. These findings illustrate that $\bullet\text{O}_2^-$ is the major active

species, followed by $\bullet\text{OH}$ and h^+ in photocatalytic degradation of TC by 3 wt%CQDs/ Bi_2WO_6 .

Moreover, it is clear that the CB potential of pure Bi_2WO_6 is 0.21 eV vs. NHE, and the e^- in the CB of Bi_2WO_6 cannot thermodynamically reduce O_2 to $\bullet\text{O}_2^-$. However, for 3 wt%CQDs/ Bi_2WO_6 , the $\bullet\text{O}_2^-$ signal is

obviously observed in the EPR analyses and quenching experiments. This result reveals that CQDs can serve as a semiconductor that occupies an appropriate CB position to reduce O_2 to $\bullet O_2^-$. The CB potential of CQDs (-1.02 eV vs. NHE) is enough to reduce O_2 to $\bullet O_2^-$. If the photo-produced e^- in the CB of CQDs could transfer to the CB of Bi_2WO_6 , under the same condition, the e^- in the CB of Bi_2WO_6 would not be capable of reducing O_2 for producing $\bullet O_2^-$. Thus, the electrons in the CB of Bi_2WO_6 would be inclined to recombine with the photoproduced h^+ in the VB of CQDs. As a result, the 3 wt% CQDs/ Bi_2WO_6 composite has a strong e^- reducibility of the CQDs CB and h^+ oxidability of the Bi_2WO_6 VB to produce abundant $\bullet O_2^-$ and $\bullet OH$, indicating the spatial separation of the photoproduced charges via an S-scheme transfer path and its ability to boost the degradation of TC under visible light.

Based on the above-presented results, a reasonable mechanism of 3 wt% CQDs/ Bi_2WO_6 S-scheme heterojunction for photocatalytic TC degradation was proposed. As displayed in Fig. 10, under light irradiation, the e^- in the VB of Bi_2WO_6 and CQDs are excited to their respective CB (Eqs. (10–11)). Because of the up-converted property of CQDs, it acts as energy converters to absorb long-wavelength light ($\lambda_1 = 600$ –850 nm) and emit shorter-wavelength light ($\lambda_2 = 400$ –600 nm). The converted short wavelength light can also make e^- in the VB of Bi_2WO_6 excited to its CB. Owing to the Bi_2WO_6 and CQDs being closely contacted by Bi-O-C bonds, the photoproduced e^- could be easily transferred from the CB of Bi_2WO_6 to the VB of CQDs and combined with h^+ under the action of IEF and energy band bending (Eq. (12)). The CB potential of CQDs is -1.02 eV vs. NHE, which is lower than that of the $O_2/\bullet O_2^-$ potential (-0.33 eV vs. NHE) [57]. Therefore, the e^- could react with O_2 on the surface of the catalyst to form $\bullet O_2^-$ (Eq. (13)). Meanwhile, the VB potential of Bi_2WO_6 is 2.91 eV vs. NHE, which is higher than that of the $OH^-/\bullet OH$ potential (1.99 eV vs. NHE) [58] and $H_2O/\bullet OH$ potential (2.38 eV vs. NHE) [59]. Thus, the h^+ in the VB of the Bi_2WO_6 can oxidize H_2O/OH^- to $\bullet OH$ (Eq. (14)). Besides, the h^+ itself is also an active species that can directly attack TC. Finally, $\bullet O_2^-$, $\bullet OH$, and h^+ all react with TC to generate CO_2 , H_2O , and small molecules (Eq. (15)). To sum up, the possible mechanism of the degradation process under visible light is shown as follows:



3.5. Possible intermediates and degradation pathways of TC

To elucidate the degradation mechanism and reactive sites of TC, LC-MS analysis and Fukui function calculations were carried out. The total MS spectra of possible molecular intermediates at several reaction times (0, 20, 40 min) are shown in Fig. S16. The peak intensity of the TC ($m/z = 445$) is gradually reduced with increasing irradiation time. However, the peak intensity of the molecules with smaller m/z values is first increased and then decreased upon further irradiation time, which reveals that TC is gradually decomposed into small molecules by 3 wt% CQDs/ Bi_2WO_6 and further mineralized. The optimized TC molecule is presented in Fig. 11a, and the calculated Fukui index is listed in Fig. S17. According to Fukui function calculation, the 9 C, 20 O, 23 O, 26 O, 28 N, and 29 C positions display high f^- values, indicating the potential for h^+ attack; the 2 C, 10 C, 16 C, 20 O, 23 O, and 27 O positions display high f^0 values, and so these molecular sites are anticipated to undergo preferential attack by $\bullet O_2^-$; the 2 C, 16 C, 20 O, 23 O, 26 O, and 28 N positions exhibit high f^0 values, implying that these sites can be attacked by $\bullet OH$ [60]. Additionally, the ESP distributions indicate that the regions around 32 O in the hydroxyl group, 20 O in the carbonyl group, and 25 N in the acylamine group for TC (Fig. 11b) may be attacked by the negatively charged $\bullet O_2^-$, thus facilitating interfacial reactions. Based on the LC-MS and Fukui function analysis, the probable degradation intermediates and pathways are respectively shown in Figs. S18 and 11c. In pathway I, TC undergoes N-demethylation to form P_1 ($m/z = 431$) by h^+ attack, and P_1 loses the amide group and amino group to form P_2 ($m/z = 362$) by $\bullet OH$ attack [60]. Following that, ring-opening reaction and dehydroxylation reaction occur to generate P_6 by $\bullet O_2^-$ and $\bullet OH$ attack [24,61]. In addition, P_1 opens the ring to deamidate and dehydroxylate to form P_7 ($m/z = 388$), and then the continuous double bond is broken to form P_8 ($m/z = 261$) [24]. In pathway II, TC ($m/z = 445$) is converted into P_9 ($m/z = 481$) by hydroxylation reaction caused by $\bullet OH$ attack [17]. Afterwards, P_9 undergoes deamination, demethylation reaction, and double bond cleavage to generate P_{10} ($m/z = 437$), which is gradually decomposed into small molecules with m/z of 216 via further persistent attacking of h^+ and $\bullet O_2^-$ radicals [62]. Finally, these intermediates with a molecular weight > 200 are transformed into smaller organic molecules such as P_{14} ($m/z = 149$), P_{15} ($m/z = 85$), P_{16} ($m/z = 102$), P_{17} ($m/z = 114$), P_{18} ($m/z = 91$), P_{19} ($m/z = 75$), and P_{20} ($m/z = 60$). These molecules are then mineralized into CO_2 and H_2O by $\bullet O_2^-$, $\bullet OH$ and h^+ .

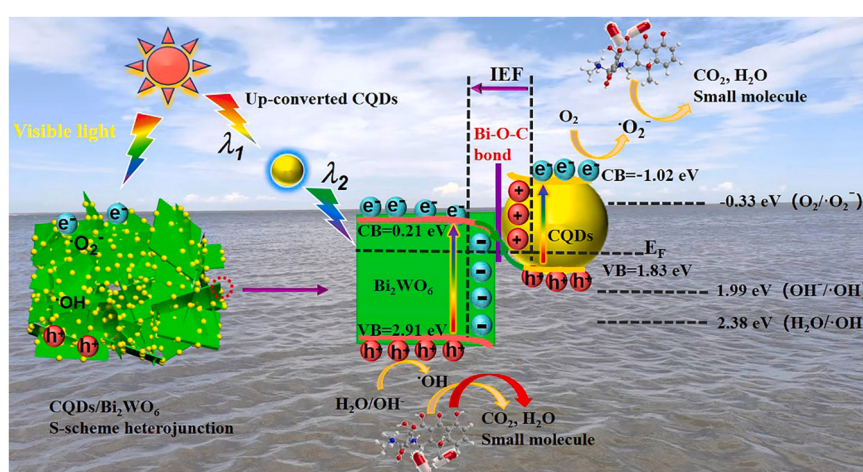


Fig. 10. Possible mechanism for the photocatalytic TC degradation over 3 wt% CQDs/ Bi_2WO_6 under visible light.

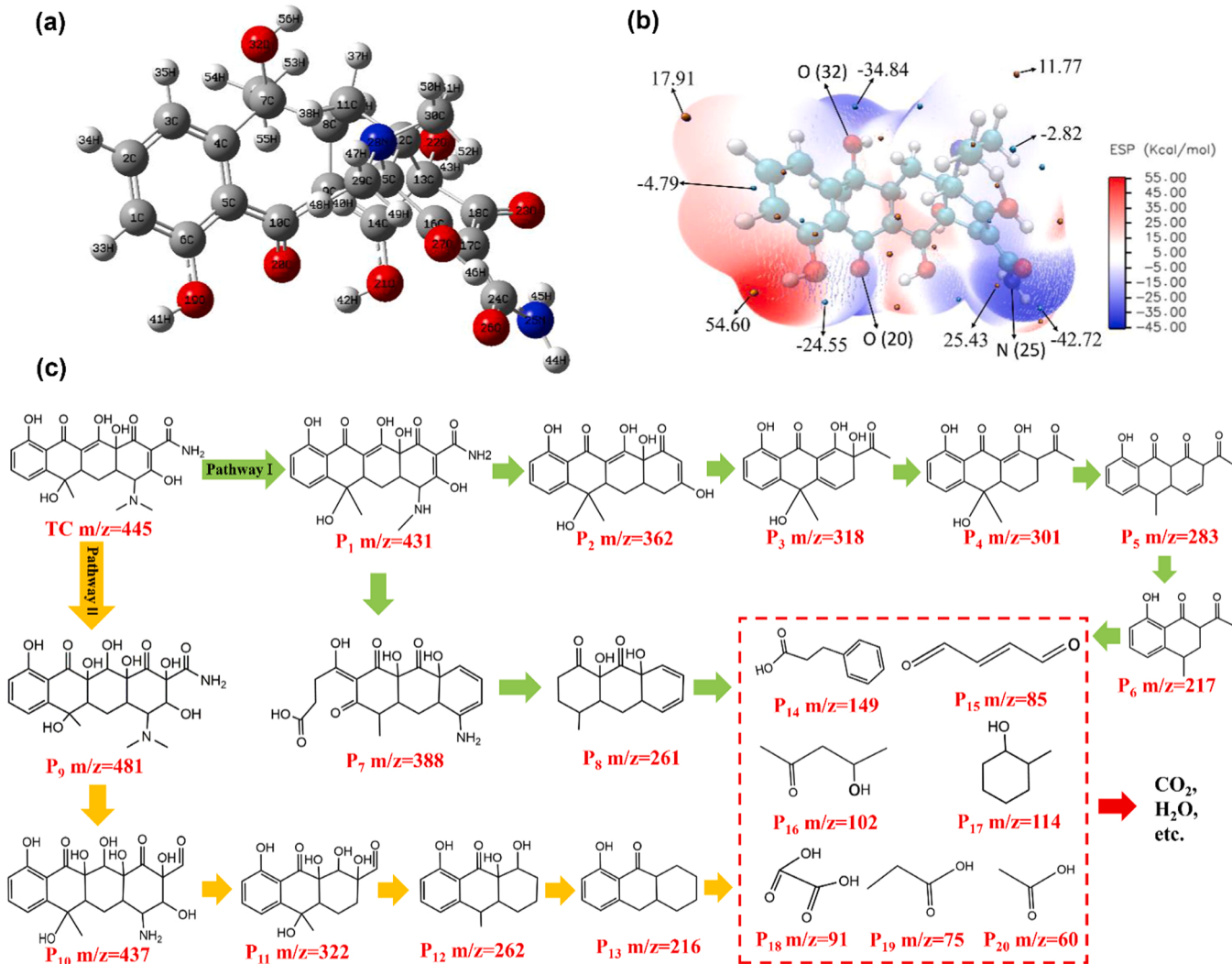


Fig. 11. (a) Optimized molecular structure of TC. (b) ESP distributions of TC. (c) The possible pathways for TC degradation by 3 wt% CQDs/Bi₂WO₆ S-scheme heterojunction under visible light.

3.6. Toxicity assessment of heterojunction and TC by-products using *E. coli* as an indicator

Toxicity actions of the 3 wt% CQDs/Bi₂WO₆ heterojunction, TC, and its photodegraded products were evaluated by highlighting their impacts on the surviving bacterial colonies density compared to that of the blank. As displayed in Fig. 12a, the addition of 3 wt% CQDs/Bi₂WO₆ heterojunction leaching solution does not remarkably vary the bacterial colonies density in comparison with the blank sample. In the same way, the growth curves of *E. coli* (Fig. 12b) demonstrate the negligible influence of 3 wt% CQDs/Bi₂WO₆ heterojunction on bacteria, suggesting that 3 wt% CQDs/Bi₂WO₆ heterojunction cannot further pollute the environment during the photocatalytic process. Fig. 12c exhibits that *E. coli* colony is not observed on the culture dishes with the introduction of primordial TC (photodegradation for 0 min). This result proves that the TC has a high inactivation effect on *E. coli*. Nevertheless, when the TC is photodegraded after a period of time, their toxicity actions on the *E. coli* dramatically decline. Significantly, compared to the blank group, the toxicity action of the degraded TC after 40 min of photocatalytic reaction on the growth of *E. coli* is negligible, indicating that 3 wt% CQDs/Bi₂WO₆ heterojunction can considerably disintegrate TC into less toxic intermediates, CO₂ or H₂O after 40 min of light exposure. The aforementioned findings show the great potential of photocatalytic degradation of TC using 3 wt% CQDs/Bi₂WO₆ heterojunction for

environment-friendly and safe application in real wastewater purification.

4. Conclusions

In conclusion, novel S-scheme CQDs/Bi₂WO₆ heterojunctions were constructed by adding CQDs derived from waste biomass into the hydrothermal synthesis system of Bi₂WO₆. The interfacial interaction of the Bi-O-C bonds between CQDs and Bi₂WO₆ was formed, which can make heterojunction more stable and provide an atomic-level interfacial channel for boosting charge separation. Theoretical calculations, in-situ XPS, and EPR analysis demonstrate the S-scheme charge migration pathway in the 3 wt% CQDs/Bi₂WO₆ catalyst system. The high redox ability, enhanced visible light absorption ($\lambda \leq 850$ nm), and effective separation and migration of the photoproduced charges greatly boost the photocatalytic efficiency of the 3 wt% CQDs/Bi₂WO₆ S-scheme heterojunction. Consequently, the photodegradation efficiency of TC by 3 wt% CQDs/Bi₂WO₆ heterojunction reaches 89.0% within 40 min, and the degradation rate constant is 4.01 and 64.71 times more than those of pure Bi₂WO₆ and CQDs, respectively. Furthermore, 3 wt% CQDs/Bi₂WO₆ heterojunction exhibited favorable adaptability in real water and high stability in recycling experiments. The photocatalytic mechanism, two degradation pathways, and possible intermediates were proposed based on DFT calculations and experimental results. Moreover,

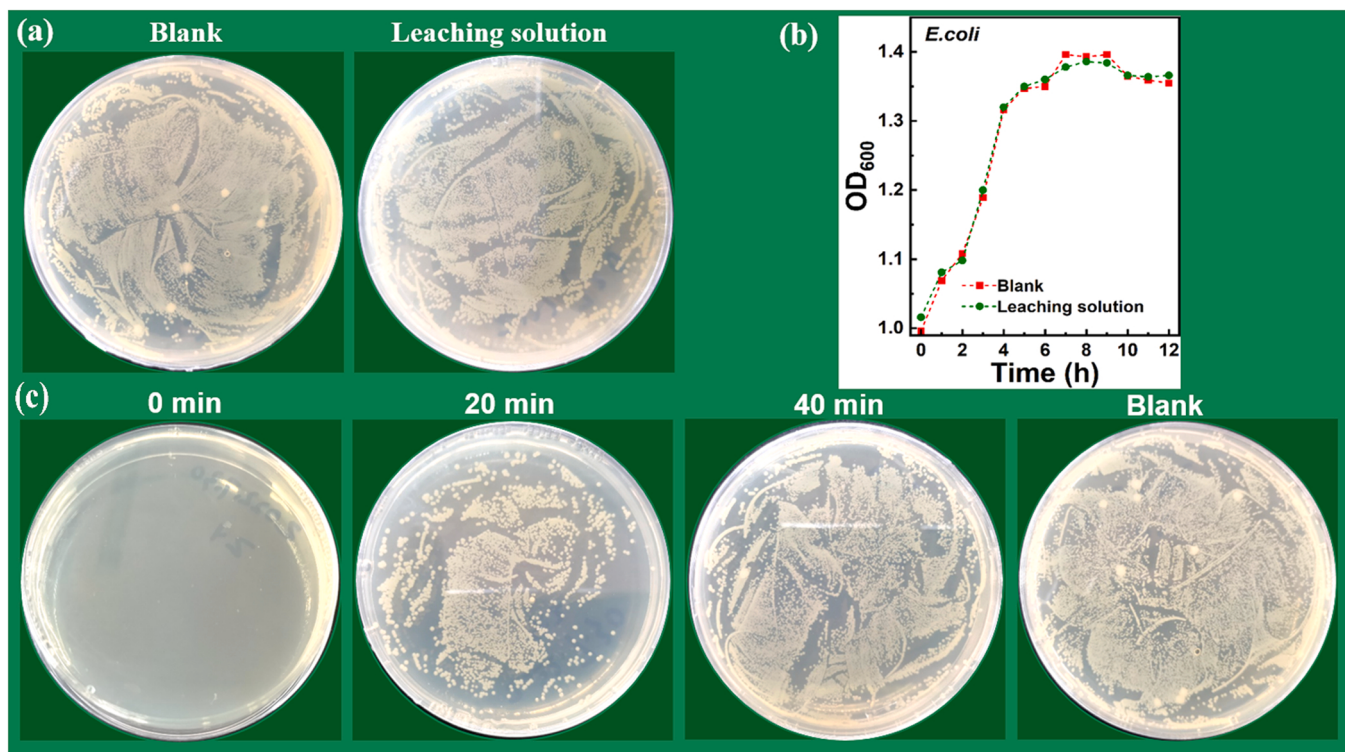


Fig. 12. (a) Photographs of *E. coli* colonies formed on LB-agar plates with and without 3 wt% CQDs/Bi₂WO₆ heterojunction leaching solution addition. (b) Growth curves of *E. coli* obtained after adding 3 wt% CQDs/Bi₂WO₆ heterojunction leaching solution for 12 h. (c) Photographs of *E. coli* colonies formed on LB-agar plates with the addition of TC solutions treated in the 3 wt% CQDs/Bi₂WO₆ heterojunction at different times under visible light (0, 20 and 40 min), and blank (without TC).

the non-toxicity of the 3 wt% CQDs/Bi₂WO₆ heterojunction and the by-products of TC degradation were attested by *E. coli* cultivation, which further evidences the feasibility of the 3 wt% CQDs/Bi₂WO₆ heterojunction to treat wastewater. This work gives meaningful insight into the design of efficient photocatalysts with chemically bonded, green, and low-cost S-scheme heterojunction for purifying antibiotics-containing wastewater.

CRediT authorship contribution statement

Haitao Ren: Experimental, Data curation, Methodology, Writing – original draft preparation. **Fan Qi:** Formal analysis, Software. **Abdelkader Labidi:** Writing – review & editing. **Junjun Zhao:** Biotoxicity assessment. **Hui Wang:** Validation, Visualization. **Yue Xin:** Investigation. **Jianmin Luo:** Supervision, Writing – review & editing. **Chuanyi Wang:** Supervision, Writing – review & editing, Project administration, Funding acquisition.

Declaration of Competing Interest

The authors declare that they have no known competing financial interests or personal relationships that could have appeared to influence the work reported in this paper.

Data availability

The authors do not have permission to share data.

Acknowledgments

This work was supported by the National Natural Science Foundation of China (52161145409 and 21976116), Shaanxi Science and Technology Program (2020KZW-005), SAEA of China ("Belt and Road" Innovative Exchange Foreign Expert Project DL2021041001L, and

Foreign Young Talent Program QN2021041003L).

Appendix A. Supporting information

Supplementary data associated with this article can be found in the online version at [doi:10.1016/j.apcatb.2023.122587](https://doi.org/10.1016/j.apcatb.2023.122587).

References

- [1] Q. Zhu, A.A. Dar, Y. Zhou, K. Zhang, J. Qin, B. Pan, J. Lin, A.O.T. Patrocino, C. Wang, Oxygen vacancies promoted piezoelectricity toward piezo-photocatalytic decomposition of tetracycline over SrBi₄Ti₄O₁₅, *ACS EST Engg.* 2 (2022) 1365–1375, <https://doi.org/10.1021/acestengg.1c00479>.
- [2] C. Huang, B. Jin, M. Han, Y. Yu, G. Zhang, H.P.H. Arp, The distribution of persistent, mobile and toxic (PMT) pharmaceuticals and personal care products monitored across Chinese water resources, *J. Hazard. Mater.* 2 (2021), 100026, <https://doi.org/10.1016/j.hazmat.2021.100026>.
- [3] F. Dong, Z. Wang, Y. Li, W.-K. Ho, S.C. Lee, Immobilization of polymeric g-C₃N₄ on structured ceramic foam for efficient visible light photocatalytic air purification with real indoor illumination, *Environ. Sci. Technol.* 48 (2014) 10345–10353, <https://doi.org/10.1021/es502290f>.
- [4] T. Chen, L. Liu, C. Hu, H. Huang, Recent advances on Bi₂WO₆ based photocatalysts for environmental and energy applications, *Chin. J. Catal.* 42 (2021) 1413–1438, [https://doi.org/10.1016/S1872-2067\(20\)63769-X](https://doi.org/10.1016/S1872-2067(20)63769-X).
- [5] J. Di, J. Xia, Y. Ge, H. Li, H. Ji, H. Xu, Q. Zhang, H. Li, M. Li, Novel visible-light-driven CQDs/Bi₂WO₆ hybrid materials with enhanced photocatalytic activity toward organic pollutants degradation and mechanism insight, *Appl. Catal. B Environ.* 168 169 (2015) 51–61, <https://doi.org/10.1016/j.apcatb.2014.11.057>.
- [6] J. Hu, D. Chen, Z. Mo, N. Li, Q. Xu, H. Li, J. He, H. Xu, J. Lu, Z-Scheme 2D/2D heterojunction of black phosphorus/monolayer Bi₂WO₆ nanosheets with enhanced photocatalytic activities, *Angew. Chem. Int. Ed.* 58 (2019) 2073–2077, <https://doi.org/10.1002/ange.201813417>.
- [7] Z. Li, S. Chen, Z. Li, J. Sun, J. Yang, J. Wei, S. Wang, H. Song, Y. Hou, Visible light driven antibiotics degradation using S-scheme Bi₂WO₆/CoIn₂S₄ heterojunction: Mechanism, degradation pathways and toxicity assessment, *Chemosphere* 303 (2022), 135113, <https://doi.org/10.1016/j.chemosphere.2022.135113>.
- [8] H. Huang, C. Zhou, X. Jiao, H. Yuan, J. Zhao, C. He, J. Hofkens, M.B.J. Roeflaers, J. Long, J.A. Steele, Subsurface Defect Engineering in Single-Unit-Cell Bi₂WO₆ Monolayers Boosts Solar-Driven Photocatalytic Performance, *ACS Catal.* 10 (2019) 1439–1443, <https://doi.org/10.1021/acscatal.9b04789>.
- [9] Y. Liu, L. Chen, Q. Yuan, J. He, C.-T. Au, S.-F. Yin, A green and efficient photocatalytic route for the highly-selective oxidation of saturated alpha-carbon C-

H bonds in aromatic alkanes over flower-like Bi_2WO_6 , *Chem. Commun.* 52 (2016) 1274–1277, <https://doi.org/10.1039/C5CC07586F>.

[10] G. Liu, Y. Huang, H. Lv, H. Wang, Y. Zeng, M. Yuan, Q. Meng, C. Wang, Confining Single-atom Pd on $\text{g-C}_3\text{N}_4$ with Carbon Vacancies towards Enhanced Photocatalytic NO Conversion, *Appl. Catal. B Environ.* 84 (2021) 2119683, <https://doi.org/10.1016/j.apcatb.2020.119683>.

[11] P. Zhang, X.W. Lou, Design of heterostructured hollow photocatalysts for solar to chemical energy conversion, *Adv. Mater.* 31 (2019), 1900281, <https://doi.org/10.1002/adma.201900281>.

[12] S. Wageh, A.A. Al-Ghamdi, R. Jafer, X. Li, P. Zhang, A new heterojunction in photocatalysis: S-scheme heterojunction, *Chin. J. Catal.* 42 (2021) 667–669, [https://doi.org/10.1016/s1872-2067\(20\)63705-6](https://doi.org/10.1016/s1872-2067(20)63705-6).

[13] Q. Xu, L. Zhang, B. Cheng, J. Fan, J. Yu, S-scheme heterojunction photocatalyst, *Chem* 6 (2020) 1543–1559, <https://doi.org/10.1016/j.chempr.2020.06.010>.

[14] L. Wang, C. Bie, J. Yu, Challenges of Z-scheme photocatalytic mechanisms, *Trends Chem.* 4 (2022) 973–983, <https://doi.org/10.1016/j.trechm.2022.08.008>.

[15] L. Zhang, J. Zhang, H. Yu, J. Yu, Emerging S-scheme photocatalyst, *Adv. Mater.* 34 (2022), 2107668, <https://doi.org/10.1002/adma.202107668>.

[16] Y. Su, X. Xu, R. Li, X. Luo, H. Yao, S. Fang, K.P. Homewood, Z. Huang, Y. Gao, X. Chen, Design and fabrication of a CdS QDs/ Bi_2WO_6 monolayer S-scheme heterojunction configuration for highly efficient photocatalytic degradation of trace ethylene in air, *Chem. Eng. J.* 429 (2022), 132241, <https://doi.org/10.1016/j.cej.2021.132241>.

[17] S. Li, M. Cai, Y. Liu, C. Wang, R. Yan, X. Chen, Constructing $\text{Cd}_{0.5}\text{Zn}_{0.5}\text{S}/\text{Bi}_2\text{WO}_6$ S-scheme heterojunction for boosted photocatalytic antibiotic oxidation and Cr (VI) reduction, *Adv. Powder Mater.* 2 (2023), 100073, <https://doi.org/10.1016/j.apmatc.2022.100073>.

[18] J. Wang, H. Cheng, D. Wei, Z. Li, Ultrasonic-assisted fabrication of $\text{Cs}_2\text{AgBiBr}_6/\text{Bi}_2\text{WO}_6$ S-scheme heterojunction for photocatalytic CO_2 reduction under visible light, *Chin. J. Catal.* 43 (2022) 2606–2614, [https://doi.org/10.1016/S1872-2067\(22\)64091-9](https://doi.org/10.1016/S1872-2067(22)64091-9).

[19] X. Lian, W. Xue, S. Dong, E. Liu, H. Li, K. Xu, Construction of S-scheme $\text{Bi}_2\text{WO}_6/\text{g-C}_3\text{N}_4$ heterostructure nanosheets with enhanced visible-light photocatalytic degradation for ammonium dinitramide, *J. Hazard. Mater.* 412 (2021), 125217, <https://doi.org/10.1016/j.jhazmat.2021.125217>.

[20] R.B. González-González, A. Sharma, R. Parra-Saldivar, R.A. Ramirez-Mendoza, M. Bilal, H.M.N. Iqbal, Decontamination of emerging pharmaceutical pollutants using carbon-dots as robust materials, *J. Hazard. Mater.* 423 (2022), 127145, <https://doi.org/10.1016/j.jhazmat.2021.127145>.

[21] B. Wang, Z. Deng, Z. Li, Efficient chemoselective hydrogenation of nitrobenzene to aniline, azoxybenzene and azobenzene over CQDs/ ZnIn_2S_4 nanocomposites under visible light, *J. Catal.* 389 (2020) 241–246, <https://doi.org/10.1016/j.jcat.2020.05.041>.

[22] Y. Zhang, Y. Li, Y. Yuan, Carbon Quantum Dot-Decorated $\text{BiOBr}/\text{Bi}_2\text{WO}_6$ Photocatalytic Micromotor for Environmental Remediation and DFT Calculation, *ACS Catal.* 12 (2022) 13897–13909, <https://doi.org/10.1021/acscatal.2c04149>.

[23] F. Wang, Y. Wang, Y. Wu, D. Wei, L. Li, Q. Zhang, H. Liu, Y. Liu, W. Lv, G. Liu, Template-free synthesis of oxygen-containing ultrathin porous carbon quantum dots/ $\text{g-C}_3\text{N}_4$ with superior photocatalytic activity for PPCPs remediation, *Environ. Sci. Nano* 6 (2019) 2565–2576, <https://doi.org/10.1039/c9en00509a>.

[24] P. Peng, Z. Chen, X. Li, Y. Wu, Y. Xia, A. Duan, D. Wang, Q. Yang, Biomass-derived carbon quantum dots modified $\text{Bi}_2\text{MoO}_6/\text{Bi}_2\text{S}_3$ heterojunction for efficient photocatalytic removal of organic pollutants and Cr (VI), *Sep. Purif. Technol.* 291 (2022), 120901, <https://doi.org/10.1016/j.seppur.2022.120901>.

[25] D.S. Achilleos, W. Yang, H. Kasap, A. Savateev, Y. Markushyna, J.R. Durrant, E. Reisner, Solar reforming of biomass with homogeneous carbon dots, *Angew. Chem. Int. Ed.* 59 (2020) 18184–18188, <https://doi.org/10.1002/anie.202008217>.

[26] Y. Zhou, E. Zahran, B. Quiroga, J. Perez, K. Mintz, Z. Peng, P.Y. Liyanage, R. R. Pandey, C.C. Chusuei, R.M. Leblanc, Size-dependent photocatalytic activity of carbon dots with surface-state determined photoluminescence, *Appl. Catal. B Environ.* 248 (2019) 157–166, <https://doi.org/10.1016/j.apcatb.2019.02.019>.

[27] F. Qin, Y. Ma, S. Zheng, C. Hu, L. Wei, R. Yang, Y. Ma, C. Zhang, Construction of novel Z-Scheme N-CQDs/ Sn_3O_4 heterojunction for excellent photocatalytic degradation of organic pollutant, *J. Clust. Sci.* 33 (2022) 913–923, <https://doi.org/10.1007/s10876-021-02020-9>.

[28] F. Wang, Y. Wu, Y. Wang, J. Li, X. Jin, Q. Zhang, R. Li, S. Yan, H. Liu, Y. Feng, G. Liu, W. Lv, Construction of novel Z-scheme nitrogen-doped carbon dots/ TiO_2 nanosheet photocatalysts for broad-spectrum-driven diclofenac degradation: Mechanism insight, products and effects of natural water matrices, *Chem. Eng. J.* 356 (2019) 857–868, <https://doi.org/10.1016/j.cej.2018.09.092>.

[29] G. Huang, L. Liu, L. Chen, L. Gao, J. Zhu, H. Fu, Unique insights into photocatalytic VOCs oxidation over WO_3 /carbon dots nanohybrid assisted by water activation and electron transfer at interfaces, *J. Hazard. Mater.* 423 (2022), 127134, <https://doi.org/10.1016/j.jhazmat.2021.127134>.

[30] J. Diaz-Angulo, J. Lara-Ramos, M. Mueses, A. Hernández-Ramírez, G. Li Puma, F. Machuca-Martínez, Enhancement of the oxidative removal of diclofenac and of the TiO_2 rate of photon absorption in dye-sensitized solar pilot scale CPC photocatalytic reactors, *Chem. Eng. J.* 381 (2020) 12252, <https://doi.org/10.1016/j.cej.2019.122520>.

[31] G. Li Puma, V. Puddu, H.K. Tsang, A. Gora, B. Toepfer, Photocatalytic oxidation of multicomponent mixtures of estrogens (estrone (E1), 17 β -estradiol (E2), 17 β -ethynodiol (EE2) and estradiol (E3)) under UVA and UVC radiation: Photon absorption, quantum yields and rate constants independent of photon absorption, *Appl. Catal. B Environ.* 99 (2010) 388–397, <https://doi.org/10.1016/j.apcatb.2010.05.015>.

[32] B. Wang, Z. Li, H. Ma, J. Zhang, L.Y. Jiao, H. Hao, E.Z. Liu, L. Xu, C. Wang, B. Zhou, X.X. Ma, Dynamic construction of self-assembled supramolecular $\text{H}_2\text{SubPcB-OPhCOOH/Ag}_3\text{PO}_4$ S-scheme arrays for visible photocatalytic oxidation of antibiotics, *Appl. Catal. B Environ.* 318 (2022), 121882, <https://doi.org/10.1016/j.apcatb.2022.121882>.

[33] R. Acosta-Herazo, M.Á. Mueses, G. Li Puma, F. Machuca-Martínez, Impact of photocatalyst optical properties on the efficiency of solar photocatalytic reactors rationalized by the concepts of initial rate of photon absorption (IRPA) dimensionless boundary layer of photon absorption and apparent optical thickness, *Chem. Eng. J.* 356 (2019) 839–849, <https://doi.org/10.1016/j.cej.2018.09.085>.

[34] Q.Y. Wei, Y. Wang, B. Dai, Y. Yang, H.J. Liu, H.J. Yuan, D.W. Jing, L. Zhao, Theoretical study on flow and radiation in tubular solar photocatalytic reactor, *Front. Energy* 15 (2021) 687–699, <https://doi.org/10.1007/s11708-021-0773-9>.

[35] I. Grčić, G. Li Puma, Six-flux absorption-scattering models for photocatalysis under wide-spectrum irradiation sources in annular and flat reactors using catalysts with different optical properties, *Appl. Catal. B Environ.* 211 (2017) 222–234, <https://doi.org/10.1016/j.apcatb.2017.04.014>.

[36] R. Acosta-Herazo, J. Monterroza-Romero, M.Á. Mueses, F. Machuca-Martínez, G. Li Puma, Coupling the Six Flux Absorption-Scattering Model to the Heney-Greenstein scattering phase function: evaluation and optimization of radiation absorption in solar heterogeneous photoreactors, *Chem. Eng. J.* 302 (2016) 86–96, <https://doi.org/10.1016/j.cej.2016.04.127>.

[37] J. Wang, J. Wang, N. Li, X. Du, J. Ma, C. He, Z. Li, Direct Z-Scheme 0D/2D Heterojunction of CsPbBr_3 Quantum Dots/ Bi_2WO_6 Nanosheets for Efficient Photocatalytic CO_2 Reduction, *ACS Appl. Mater. Interfaces* 12 (2020) 31477–31485, <https://doi.org/10.1021/acsmi.0c08152>.

[38] Z. Zhu, H. Huang, L. Liu, F. Chen, N. Tian, Y. Zhang, H. Yu, Chemically Bonded $\alpha\text{-Fe}_2\text{O}_3/\text{Bi}_4\text{MO}_8\text{Cl}$ Dot-on-Plate Z-Scheme Junction with Strong Internal Electric Field for Selective Photooxidation of Aromatic Alcohols, *Angew. Chem. Int. Ed.* 61 (2022), e202203519, <https://doi.org/10.1002/anie.202203519>.

[39] Y. Cui, T. Wang, J. Liu, L. Hu, Q. Nie, Z. Tan, H. Yu, Enhanced solar photocatalytic degradation of nitric oxide using graphene quantum dots/bismuth tungstate composite catalysts, *Chem. Eng. J.* 420 (2021), 129595, <https://doi.org/10.1016/j.cej.2021.129595>.

[40] J. Zhang, X. Yuan, L. Jiang, Z. Wu, X. Chen, H. Wang, H. Wang, G. Zeng, Highly efficient photocatalysis toward tetracycline of nitrogen doped carbon quantum dots sensitized bismuth tungstate based on interfacial charge transfer, *J. Colloid Interface Sci.* 511 (2018) 296–306, <https://doi.org/10.1016/j.jcis.2017.09.083>.

[41] Y. Wu, H. Ji, Q. Liu, Z. Sun, P. Li, P. Ding, M. Guo, X. Yi, W. Xu, C.-C. Wang, S. Gao, Q. Wang, W. Liu, S. Chen, Visible light photocatalytic degradation of sulfanilamide enhanced by Mo doping of BiOBr nanoflowers, *J. Hazard. Mater.* 424 (2022), 127563, <https://doi.org/10.1016/j.jhazmat.2021.127563>.

[42] Z. Zheng, H. Li, X. Zhang, H. Jiang, X. Geng, S. Li, H. Tu, X. Cheng, P. Yang, Y. Wan, High-absorption solar steam device comprising $\text{Au}@\text{Bi}_2\text{MoO}_6$ -CDs: Extraordinary desalination and electricity generation, *Nano Energy* 68 (2019), 104298, <https://doi.org/10.1016/j.nanoen.2019.104298>.

[43] Q. Zhao, L. Liu, S. Li, R. Liu, Built-in electric field-assisted charge separation over carbon dots-modified Bi_2WO_6 nanoplates for photodegradation, *Appl. Surf. Sci.* 465 (2018) 164–171, <https://doi.org/10.1016/j.apsusc.2018.09.168>.

[44] B. Pan, Y. Wu, B. Rhimi, J. Qin, Y. Huang, M. Yuan, C. Wang, Oxygen-doping of ZnIn_2S_4 nanosheets towards boosted photocatalytic CO_2 reduction, *J. Energy Chem.* 57 (2021) 1–9, <https://doi.org/10.1016/j.jec.2020.08.024>.

[45] A. Wang, W. Hong, L. Li, R. Guo, Y. Xiang, Y. Ye, G. Zou, H. Hou, X. Ji, Hierarchical bismuth composite for fast lithium storage: Carbon dots tuned interfacial interaction, *Energy Storage Mater.* 44 (2022) 145–155, <https://doi.org/10.1016/j.ensm.2021.10.019>.

[46] W. Li, X. Wang, Q. Ma, F. Wang, X. Chu, X. Wang, C. Wang, CdS@h-BN heterointerface construction on reduced graphene oxide nanosheets for hydrogen production, *Appl. Catal. B Environ.* 284 (2021), 119688, <https://doi.org/10.1016/j.apcatb.2020.119688>.

[47] S. Wang, L. Li, Z. Zhu, M. Zhao, L. Zhang, N. Zhang, Q. Wu, X. Wang, G. Li, Remarkable Improvement in Photocatalytic Performance for Tannery Wastewater Processing via SnS_2 Modified with N-Doped Carbon Quantum Dots: Synthesis, Characterization, and 4-Nitrophenol-Aided Cr (VI) Photoreduction, *Small* 19 (2019), 1804515, <https://doi.org/10.1002/smll.201804515>.

[48] K. Li, Y. Jiang, W. Rao, Y. Li, X. Liu, J. Zhang, X. Xu, K. Lin, Cooperative coupling strategy for constructing 0D/2D carbon nitride composites with strengthened chemical interaction for enhanced photocatalytic applications, *Chem. Eng. J.* 431 (2022), 134075, <https://doi.org/10.1016/j.cej.2021.134075>.

[49] J. Guo, H. Sun, X. Yuan, L. Jiang, Z. Wu, H. Yu, N. Tang, M. Yu, M. Yan, J. Liang, Photocatalytic degradation of persistent organic pollutants by Co-Cl bond reinforced $\text{CoAl-LDH}/\text{Bi}_{12}\text{O}_{17}\text{C}_2$ photocatalyst: mechanism and application prospect evaluation, *Water Res.* 219 (2022), 118558, <https://doi.org/10.1016/j.watres.2022.118558>.

[50] Z. Wang, C. Lai, L. Qin, Y. Fu, J. He, D. Huang, B. Li, M. Zhang, S. Liu, L. Li, W. Zhang, H. Yi, X. Liu, X. Zhou, ZIF-8-modified MnFe_2O_4 with high crystallinity and superior photo-Fenton catalytic activity by Zn-O-Fe structure for TC degradation, *Chem. Eng. J.* 392 (2020), 124851, <https://doi.org/10.1016/j.cej.2020.124851>.

[51] Z. Zhang, R. Ji, Q. Sun, J. He, D. Chen, N. Li, H. Li, A. Marcomini, Q. Xu, J. Lu, Enhanced photocatalytic degradation of 2-chlorophenol over Z-scheme heterojunction of CdS -decorated oxygen-doped $\text{g-C}_3\text{N}_4$ under visible-light, *Appl. Catal. B Environ.* 324 (2023), 122276, <https://doi.org/10.1016/j.apcatb.2022.122276>.

[52] T. Zhou, L. Wang, X. Huang, J. Unruangsri, H. Zhang, R. Wang, Q. Song, Q. Yang, W. Li, C. Wang, K. Takahashi, H. Xu, J. Guo, PEG-stabilized coaxial stacking of two-

dimensional covalent organic frameworks for enhanced photocatalytic hydrogen evolution, *Nat. Commun.* 12 (2021) 3934, <https://doi.org/10.1038/s41467-021-24179-5>.

[53] Y. Wang, X. Liu, J. Liu, B. Han, X. Hu, F. Yang, Z. Xu, Y. Li, S. Jia, Z. Li, Carbon quantum dot implanted graphite carbon nitride nanotubes: excellent charge separation and enhanced photocatalytic hydrogen evolution, *Angew. Chem. Int. Ed.* 57 (2018) 5765–5771, <https://doi.org/10.1002/anie.201802014>.

[54] J. Li, Z. Li, X. Liu, C. Li, Y. Zheng, K.W.K. Yeung, Z. Cui, Y. Liang, S. Zhu, W. Hu, Y. Qi, T. Zhang, X. Wang, S. Wu, Interfacial engineering of $\text{Bi}_2\text{S}_3/\text{Ti}_3\text{C}_2\text{Tx}$ MXene based on work function for rapid photo-excited bacteria-killing, *Nat. Commun.* 12 (2021) 1224, <https://doi.org/10.1038/s41467-021-21435-6>.

[55] R. Shen, L. Zhang, N. Li, Z. Lou, T. Ma, P. Zhang, Y. Li, X. Li, W-N Bonds Precisely Boost Z-Scheme Interfacial Charge Transfer in $\text{g-C}_3\text{N}_4/\text{WO}_3$ Heterojunctions for Enhanced Photocatalytic H_2 Evolution, *ACS Catal.* 12 (2022) 9994–10003, <https://doi.org/10.1021/acscatal.2c02416>.

[56] Z. Wang, X. Cai, X. Xie, S. Li, X. Zhang, Z. Wang, Visible-LED-light-driven photocatalytic degradation of ofloxacin and ciprofloxacin by magnetic biochar modified flower-like Bi_2WO_6 : The synergistic effects, mechanism insights and degradation pathways, *Sci. Total Environ.* 764 (2021), 142879, <https://doi.org/10.1016/j.scitotenv.2020.142879>.

[57] X.-Q. Qiao, Z.-W. Zhang, Q.-H. Li, D. Hou, Q. Zhang, J. Zhang, D.-S. Li, P. Feng, X. Bu, In situ synthesis of n–n Bi_2MoO_6 & Bi_2S_3 heterojunctions for highly efficient photocatalytic removal of Cr(VI), *J. Mater. Chem. A* 6 (2018) 22580–22589, <https://doi.org/10.1039/C8TA08294D>.

[58] Y. Yang, D. Zhang, J. Fan, Y. Liao, Q. Xiang, Construction of an Ultrathin S Scheme Heterojunction Based on Few-Layer $\text{g-C}_3\text{N}_4$ and Monolayer $\text{Ti}_3\text{C}_2\text{Tx}$ MXene for Photocatalytic CO_2 Reduction, *Sol. RRL* 5 (2021), 2000351, <https://doi.org/10.1002/solr.202000351>.

[59] X. Li, Y. Qiu, Z. Zhu, H. Zhang, D. Yin, Novel recyclable Z-scheme $\text{g-C}_3\text{N}_4/\text{carbon nanotubes}/\text{Bi}_{25}\text{FeO}_{40}$ heterostructure with enhanced visible-light photocatalytic performance towards tetracycline degradation, *Chem. Eng. J.* 429 (2022), 132130, <https://doi.org/10.1016/j.cej.2021.132130>.

[60] R. Duan, S. Ma, S. Xu, B. Wang, M. He, G. Li, H. Fu, P. Zhao, Soybean straw biochar activating peroxydisulfate to simultaneously eliminate tetracycline and tetracycline resistance bacteria: Insights on the mechanism, *Water Res.* 218 (2022), 118489, <https://doi.org/10.1016/j.watres.2022.118489>.

[61] M. Preeyanghaa, V. Vinesh, P. Sabarikirishwaran, A. Rajkamal, M. Ashokkumar, B. Neppolian, Investigating the role of ultrasound in improving the photocatalytic ability of CQD decorated boron-doped $\text{g-C}_3\text{N}_4$ for tetracycline degradation and first-principles study of nitrogen-vacancy formation, *Carbon* 192 (2022) 405–417, <https://doi.org/10.1016/j.carbon.2022.03.011>.

[62] H. Dong, X. Zhang, J. Li, P. Zhou, S. Yu, N. Song, C. Liu, G. Che, C. Li, Construction of morphology-controlled nonmetal 2D/3D homojunction towards enhancing photocatalytic activity and mechanism insight, *Appl. Catal. B Environ.* 263 (2020), 118270, <https://doi.org/10.1016/j.apcatb.2019.118270>.